Chemical Engineering Journal 465 (2023) 142987

Contents lists available at ScienceDirect

Chemical Engineering Journal

journal homepage: www.elsevier.com/locate/cej

Tailoring MOF structure via iron decoration to enhance ORR in alkaline polymer electrolyte membrane fuel cells

Williane da Silva Freitas [a], Alessandra D'Epifanio [a,*], Carmelo Lo Vecchio [b], Irene Gatto [b], Vincenzo Baglio [b], Valerio C.A. Ficca [c], Ernesto Placidi [c], Barbara Mecheri [a,*]

[a] Department of Chemical Science and Technologies, University of Rome Tor Vergata, Via della Ricerca Scientifica, 00133 Rome, Italy
[b] Istituto di Tecnologie Avanzate per l'Energia "Nicola Giordano" (ITAE), Consiglio Nazionale delle Ricerche (CNR), Via Salita S. Lucia sopra Contesse 5, Messina 98126, Italy
[c] Department of Physics, Sapienza University of Rome, Piazzale Aldo Moro 2, 00185 Rome, Italy

ARTICLE INFO

Keywords:
Platinum-group-metal-free electrocatalysts
Metal-organic frameworks
Fe-N_x-C active sites
Oxygen reduction
Alkaline polymer electrolyte membrane fuel cell

ABSTRACT

Fe-N-C catalysts were synthesized by combining a Zn-based zeolitic imidazolate framework (ZIF-8) structure, adopted as a nitrogen-carbon template, with an iron salt and conductive carbon support followed by a thermal treatment. The effect of three different pyrolysis temperatures (700, 900, and 1000 °C) on Zn removal from ZIF-8 was investigated to enhance the formation of Fe-based moieties in the N_x-C groups during carbonization. Electrochemical characterization using a rotating ring disk electrode in an alkaline electrolyte demonstrated that ORR activity increased as the pyrolysis temperature increased. This trend can be ascribed to a more effective Zn removal and formation of high-active iron- and nitrogen-based catalytic sites, as pointed out by the Fe-N-C materials' chemical surface analysis after the pyrolysis step. The sample Fe-N-C-1000 demonstrated a remarkable ORR activity, even higher than Pt/C taken as reference.

When subjected to accelerated stress tests, the Fe-N-C-1000 sample displayed higher performance durability over a long cycling duration (30,000 cycles) compared to Pt/C taken as control. Tests in the AEMFC fed with H_2 showed that the performance of the Fe-N-C-1000 catalyst was competitive (OCV = 0.98 *vs.* 1.05 V, 149 *vs.* 148 mW cm^{-2}) compared to the state-of-the-art Pt/C electrode, using a FUMASEP® FAA-3-50 membrane. The material found an application also in alkaline direct methanol fuel cell (ADMFC) fed with methanol solutions at high concentrations (up to 10 M) due to a high methanol tolerance, as pointed out by rotating disk electrode experiments.

1. Introduction

Alkaline polymer electrolyte fuel cells are a class of fuel cells particularly suited for reducing the industry and transportation sectors' dependence on fossil fuels [1–5]. Compared to proton-exchange membrane fuel cells, H_2-fed anion exchange membrane fuel cells (AEMFCs) and alkaline direct methanol fuel cells (ADMFC) offer several advantages, including the possibility of enhancing material stability and eliminating platinum-group metal (PGM) catalysts at the cathode side [6–8]. Despite excellent activity towards the oxygen reduction reaction (ORR) [9,10], state-of-the-art platinum is a costly and scarce metal that experiences considerable performance decrease under operating conditions, especially in ADMFC where methanol crossover through the anionic exchange membrane leads to a mixed potential at the cathode [11–13]. Therefore, there is a need to develop highly active, stable, and alcohol-tolerant PGM-free catalysts for H_2-fed AEMFCs and ADMFCs [14–17].

Atomically dispersed transition metal and nitrogen co-doped carbon (M−N−C) catalysts are among the most promising alternative to PGM catalysts due to their high ORR activity and tolerance to contaminants [11,18–26], combined with the possibility of using a wide range of precursors and synthesis approaches [27–35]. Among the transition metals, iron is the most active towards ORR [36–45]. The synthesis of Fe-N-C materials *via* pyrolysis steps leads to the formation of multitudinous N- (pyridinic-, pyrrolic-, graphitic-, quaternary- and protonated-N) and Fe-based (e.g., Fe-N_4, Fe-N_{4+1} Fe-N_{2+2}, Fe-N_2) sites differently influencing ORR activity and selectivity toward an efficient $4e^-$ or indirect electron transfer pathway ($2 \times 2e^-$) [46,47]. The proper choice of

* Corresponding authors.
E-mail addresses: alessandra.d.epifanio@uniroma2.it (A. D'Epifanio), barbara.mecheri@uniroma2.it (B. Mecheri).

https://doi.org/10.1016/j.cej.2023.142987
Received 23 February 2023; Received in revised form 10 April 2023; Accepted 12 April 2023
Available online 18 April 2023

catalyst precursors and tailoring synthesis conditions is paramount for obtaining active and stable Fe-N_x-C ORR active sites, atomically dispersed in a high surface area and porous carbon-based structure to enhance mass transport. High surface area, thermal and chemical stability, diversity of the metal center, and N-containing ligands are among the properties that render metal–organic frameworks (MOFs) attractive as M−N−C precursors [48–50]. These materials consist of a metal center joined by organic linkers to form large networks of crystalline nature. MOFs can be used in various applications, such as molecular separation, antibacterial applications, environmental remediation, and catalysis [51–54].

In a recent study, we synthesized a MOF-derived Co-N-C catalyst and investigated its applications at the cathode of both H_2-fed AEMFC and ADMFC operating with a FUMASEP® FAA-3-50 membrane. We demonstrated the electrocatalyst's exceptionally high ADMFC performance (maximum power density as high as 45 mWcm^{-2} with methanol concentration up to 10 M) outperforming Pt/C taken as control. Although competitive with other PGM-free materials (maximum power density as high as 100 mW cm^{-2}), the H_2-fed AEMFC performance was still lower than that of Pt/C [55]. We have extended our investigation to boost the MOF-based electrocatalyst's performance by tailoring the synthesis conditions to promote the formation of highly active catalytic sites based on iron as a transition metal. In this work, a zinc-based MOF ($Zn(mIm)_2$/ZIF-8) was used as a precursor to obtaining Fe-N_x-C active sites by replacing Zn with Fe during heat treatment in an inert atmosphere.

Since Zn removal from the ZIF-8 matrix is essential for forming catalytically active Fe-based moieties from the preformed N_x-C groups during carbonization [56], the electrocatalyst synthesis was optimized in terms of precursor characteristics, pyrolysis temperature, and heating rate. Tailoring the synthesis conditions enhanced the cathode performance in the H_2-fed AEMFC, while avoiding using low thermally stable nitrogen-based molecules commonly used to increase the density of Fe- and N-based active sites.

2. Material and methods

2.1. Materials

2-methylimidazole (mIm) (>98.0 %) was purchased from TCI, zinc nitrate ($Zn(NO_3)_2{\cdot}6H_2O$, 98.0 %), iron (II) acetate (>98.0 %), methanol (99.8 %), isopropanol (≥99.5 %), nitric acid (≥65.0 %), and Nafion solution (5 wt.% in lower aliphatic alcohols and water, 15–20 wt.%) were supplied by Sigma-Aldrich and the Carbon Black Pearls 2000 (BP) from CABOT. Platinum, nominally 40% on carbon black (Pt/C), was purchased by Alfa Aesar. Materials preparation and electrochemical experiments were carried out by using Millipore water (Merk, 18.2 MΩcm).

2.2. Synthesis of $Zn(mIm)_2$

6.49 g of 2-methylimidazole were dissolved in 200 mL of methanol under magnetic stirring and N_2 purging for 15 min. After that, 200 mL of a methanol solution containing 2.93 of $Zn(NO_3)_2{\cdot}6H_2O$ was poured into the previous solution (molar ratio Zn/mIm = 1/8) and kept under magnetic stirring and N_2-saturated atmosphere at room temperature (25 ± 3 °C). The colorless solution slowly turned turbid, characteristic evidence of dispersed $Zn(mIm)_2$ nanocrystals. After 2 h, the dispersion was centrifugated (7000 rpm, 15 min), and the material was collected and washed three times in fresh methanol, dried in an oven at 40 °C overnight, and grounded in a mortar, resulting in a white crystalline powder.

2.3. Fe- and N- functionalization of carbon support

The Zn removal from the ZIF-8 carbon matrix is critical to introduce Fe in the N_4-C sites of this precursor leading to formation of Fe-N_x-C active sites. For this reason, the effect of three different temperatures (700, 900 and 1000 °C) was investigated. Based on previous studies [57,58] and considering the high density of preformed N_4-C sites composing the ZIF-8 carbon matrix, a 1 wt.% of Fe (II) (nominally) was chosen as an effective content to promote formation of a high density of Fe-N_x-C active sites.

First, carbon black pearls used as conductive support were activated in concentrated nitric acid as previously described [59,60] and labeled as BP. Next, 500 mg of $Zn(mIm)_2$ precursor and 31.1 mg of iron (II) acetate were treated in an ultrasonic bath in 100 mL of methanol at room temperature for 40 min. Activated BP (490 mg) was also treated in an ultrasonic bath under the same conditions for 20 min. Then, the suspensions were mixed and stirred at room temperature for 1 h, and the resulting suspension was dried overnight at 70 °C and ground in a mortar. Finally, the catalyst precursor (800 mg) was placed in a quartz-tube furnace purged at room temperature for 20 min with Ar flowing at 200 sccm and subsequently pyrolyzed at three different temperatures (700, 900 and 1000 °C) at a heating rate of 20 °C min^{-1} for 1 h to obtain Fe-N-C-700 and Fe-N-C-900 and Fe-N-C-1000 samples.

2.4. Materials characterization

2.4.1. Physicochemical characterization

Powder X-ray diffraction (XRPD) patterns were recorded using a Philips PW1730 diffractometer equipped with a Cu X-ray tube (λ = 1.5406 Å). The morphology of the samples was investigated using a scanning electron microscope (FE-SEM, Leo Supra 35, Carl Zeiss, Oberkochen, Germany). Thermogravimetric analysis (TGA) was performed using a Mettler Toledo TGA/DSC1 Star System with the heating rate at 5, 10, and 20 °C min^{-1} in N_2 flow.

The compositional analysis was performed by means of X-ray Photoelectron Spectroscopy (XPS) using a monochromatic Al Kα (1486.6 eV) SPECS PHOIBOS 150 XPS system equipped with a 2D CMOS true counting detector. The powder samples were supported over an Au-sputtered n-type Si holder, and C, O, N, Fe, and Zn core levels were investigated for each sample along with a full survey. The spectra were processed using KolXPD software, accounting for the asymmetric shape of the graphitic sp^2-hybridized C 1s peak with a Doniach-Sunjic convoluted with a gaussian function.

2.4.2. Electrochemical characterization

Electrochemical analysis was performed using a VMP3 Potentiostat (BioLogic Science Instruments) controlled by a computer through EC-Lab V10.18 software. A standard three-electrode cell was equipped with a working electrode (either a rotating ring disk electrode RRDE AFED050P040GC, collection efficiency "*N*" = 0.26 or a RDE AFE3T050GC, Pine Research Instrumentation), a counter electrode (graphite rod, 6 mm diameter, 99.999% Sigma-Aldric), and an Ag/AgCl electrode (373/SSG/6JZ, AMEL) as the reference electrode.The potential values were measured *vs*. Ag/AgCl and converted to the reversible hydrogen electrode (RHE).

The catalyst ink was prepared as follows: 3.9 mg of catalyst were dispersed in 425 μL of isopropanol, and the suspension was ultrasonicated for 15 min at 10–15 °C. Then, 75 μL of a Nafion 0.5 wt.% solution was added to the obtained dispersion and ultrasonicated for 45 min at 15–20 °C. The working electrode was modified by dropping 5 μL of the ink onto the glassy carbon disk (0.196 cm^2) to a catalyst loading of 0.20 mg cm^{-2}. The electrode was dried in a convection oven at 40 °C for 6 min. A Pt/C ink was also prepared to a 40 μg cm^{-2} Pt/C loading (corresponding to 16 μg cm^{-2} Pt loading) and used for a performance comparison [61–63]. The catalytic layer was activated by cycling the electrode in a 1.05–0.05 V *vs*. RHE potential window at 50 mV s^{-1} (150 cycles), 150 mV s^{-1} (50 cycles), and 5 mV s^{-1} (5 cycles) in N_2-saturated KOH 0.1 M electrolyte.

Cyclic voltammetry (CV) experiments were performed to calculate the electrochemical active surface area (ECSA) of Fe-N-C and Pt/C cat-

alysts, as described in our previous work [59]. Linear sweep voltammetry (LSV) curves were recorded at a 1600 rpm electrode rotation, with the Pt ring polarized at 1.2 V *vs.* RHE. The number of electrons exchanged (n) and the hydrogen peroxide anion (HO_2^-) intermediate percentage, produced during ORR, were calculated according to Eqs. S1 and S2. By plotting *i*R-corrected potential values as a function of the logarithm of the kinetic current density (Eq. S3), Tafel plots were obtained according to Eq. S4.

Two different accelerated stress tests (AST) were carried out over 30,000 cycles to investigate durability performance. The load-cycle test was performed by cycling the potential, at a scan rate of 500 mV s^{-1}, with a square-wave ramp between 0.6 and 1.0 V *vs.* RHE holding each potential value for 3 s. For the sake of comparison with the benchmark Pt/C catalyst, the potential cycling was carried out under an N_2-saturated electrolyte, according to the D.O.E. protocol [64]. LSV-RDE measurements in an O_2-saturated electrolyte were recorded before and after to evaluate changes in performance in terms of onset (E_{onset}) and half-wave ($E_{1/2}$) potentials, limiting current density (J_{lim}), and mass activity (M.A.), which was calculated by normalizing the kinetic current density (J_k) by the active material mass loading (g cm^{-2}) on the electrode surface according to Eq. S5. The mass activity values were extrapolated at an *i*R-free voltage of 0.9 V *vs*. RHE. To evaluate the ECSA changes over cycling, triangular-wave potential CV were recorded between 0.0 and 1.05 V *vs*. RHE, in N_2-saturated electrolyte. The ECSA was calculated from CV curves referring to cycles n. 1, 1000, 5000, 10000, 15000, 20000, 25000 and 30000.

Methanol tolerance tests were carried out by LSV and Electrochemical impedance spectroscopy (EIS) at increasing aliquots of CH_3OH into the electrolyte solution to achieve 0.01, 0.05, 0.1, 1.0, and 2.0 M concentrations [65]. EIS spectra were recorded at a potential condition (half-wave potential extrapolated from the LSV curves) corresponding to the mixed kinetic + diffusion region over a frequency range of 10 kHz to 10 mHz, by applying a sinusoidal perturbation of 5 mV amplitude of the alternating current signal.

2.5. Electrodes and MEAs preparation

Electrodes and membrane-electrode assemblies (MEAs) were prepared as described in our previous work [55]. For both H_2-fed AEMFC and ADMFC, cathodes were manufactured by integrating Fe-N-C-1000 onto the Sigracet 25-BC Gas Diffusion Layer (SGL group) to a 4.5 $mgcm^{-2}$ catalyst loading, using a FAA3 ionomer (catalyst/ionomer: 80/20 wt.% ratio) [65].

For AEMFCs, the anode electrode was prepared by integrating the commercial 40 wt.% Pt/C electrocatalyst (Alfa Aesar) onto the Sigracet 25-BC Gas Diffusion Layer to a 0.5 mg cm^{-2} Pt loading, using a FAA3 ionomer (catalyst/ionomer: 80/20 wt.% ratio). The same electrode was used as a cathode to compare the Fe-N-C catalyst's performance.

For ADMFC anodes, 60 wt.% PtRu/C (Pt:Ru 1:1, Alfa Aesar) was deposited onto a Sigracet SGL35BC gas diffusion layer to a 1.5 mg cm^{-2} Pt loading, using a FAA3 ionomer (catalyst/ionomer: 80/20 wt.% ratio). An electrode based on commercial 40 wt.% Pt/C (Alfa Aesar) was prepared (same amount of ionomer and Pt loading of 1 mg cm^{-2}) and used as a cathode to compare the Fe-N-C catalyst's performance.

A Fumasep® FAA-3-50 (FuMa-Tech) in hydroxide form [66,67] was cold-assembled between the electrodes and mounted in a 5 cm^2 active area cell hardware to investigate the electrochemical behavior both in AEMFC and ADMFC.

2.6. Electrochemical characterization in AEMFCs and ADMFCs

The cell hardware was connected to a Fuel Cell Tech., Inc. test station equipped with a HP6051A electronic load.

The AEMFC performance was evaluated in terms of polarization and power density curves (60 °C operating temperature and atmospheric pressure). Fully humidified H_2 and O_2 were fed to the anode and cathode, respectively, with a flow rate set at 1.5 and 2 times the stoichiometric value.

Steady-state galvanostatic polarization experiments in ADMFC were performed at different temperatures (30 °C to 60 °C) and methanol concentrations (1 M to 10 M) in 1 M KOH, with a flow rate of 2 cm^3 min^{-1}. Fully humidified O_2 was fed at the cathode with a 100 cm^3 min^{-1} flow rate.

3. Results and discussion

Fe-N-C catalysts were prepared by using a zeolitic imidazolate framework (ZIF-8) precursor synthesized at room temperature and in a short reaction time. The ZIF-8 was used as a nitrogen and carbon source, combined with an iron salt and conductive carbon support to obtain N- and Fe-based active sites by pyrolysis treatment in an inert atmosphere. Three different pyrolysis temperatures were investigated to produce the materials labeled as Fe-N-C-700, Fe-N-C-900, and Fe-N-C-1000.

The physicochemical characterization of the precursors' materials confirmed the successful synthesis of ZIF-8 and allowed optimizing the following thermal treatment. FT-IR analysis indicates the presence of chemical bonds corresponding to the ZIF-8 structure (Fig. S1), in good agreement with the literature [68,69]. Fig. 1(a) shows the XRPD pattern of the precursors and the synthesized ZIF-8 ($Zn(mIm)_2$), compared to a reference pattern of ($Zn(mIm)_2$) from the ICSD database. The pattern of the synthesized ($Zn(mIm)_2$), different from those of the precursors, is characteristic of the highly crystalline structure of ZIF-8 as pointed out by the sharp diffraction peaks at $2\theta = 7.38°$ (0 1 1), 10.29° (0 0 2), 12.68° (1 1 2), 14.66° (0 2 2), 16.37° (0 1 3), 18.0° (2 2 2), 22.00° (1 1 4), 24.40° (2 3 3), 26.58° (1 3 4), 29.64° (0 4 4), 30.58° (3 3 4), 31.43° (2 4 4) and 32.28° (2 3 5) which correspond to the zeolite nets-sodalite (SOD) structure, in good agreement with the reference pattern and others previously reported papers [70,71].

The morphology of the synthesized ZIF-8 was investigated by SEM analysis (Fig. 1(b)), indicating particles with a diameter ranging between 50 and 100 nm well distributed as a three-dimensional net-like morphology.

To evaluate thermal stability of the synthesized ZIF and optimize the experimental conditions for the following thermal treatment necessary for the formation of ORR active sites, a thermogravimetric analysis (TGA) under N_2 atmosphere (Fig. 1(c)) was carried out using two different heating rates (5 °C min^{-1} and 20 °C min^{-1}). When the heating rate is 5 °C min^{-1} (dotted line), no significant mass change takes place below 200 °C; above 200 °C, a 5% mass loss occurs corresponding to the removal of both 2-methylimidazole (mIm) ligand and water guest molecules occluded within and adsorbed on the $Zn(mIm)_2$ surface [72].

Organic likers decomposition is observed from 500 to 600 °C (19%), followed by a higher mass loss (50%) due to carbonization of the ZIF structure, in good agreement with the literature [72,73]. It has also been found that, at this temperature range, ZnO is produced and can be further reduced to Zn(0) by carbon and removed by the matrix with the Ar flow when the temperature approaches 908 °C (zinc boiling point) [56,74]. The effect of the heating rate temperature on the $Zn(mIm)_2$ carbonization is evident when comparing the TGA profile (Fig. 1(c) and Table S1) acquired at 20 °C min^{-1} with that obtained at 5 °C min^{-1}. An increase in the heating rate shifts the onset temperatures corresponding to the organic likers decomposition to higher values consequently, the residual mass after $Zn(mIm)_2$ carbonization increases from 26% (5 °C min^{-1}) to 45 % (20 °C min^{-1}). This can be ascribed to increased temperature gradients in the sample heated at 20 °C min^{-1}, leading to increased resistance to the mass transfer of gas-phase decomposition products from condensed phases to the purge gas. As previously reported [75], this phenomenon facilitates carbonization.

Based on the body of TGA results, three different pyrolysis temperatures were selected: 700 °C, 900 °C and 1000 °C setting 20 °C min^{-1} as a heating rate for it contributes to preserving the ZIF-8 carbon matrix. The samples obtained after pyrolysis were labeled as Fe-N-C-700, Fe-N-

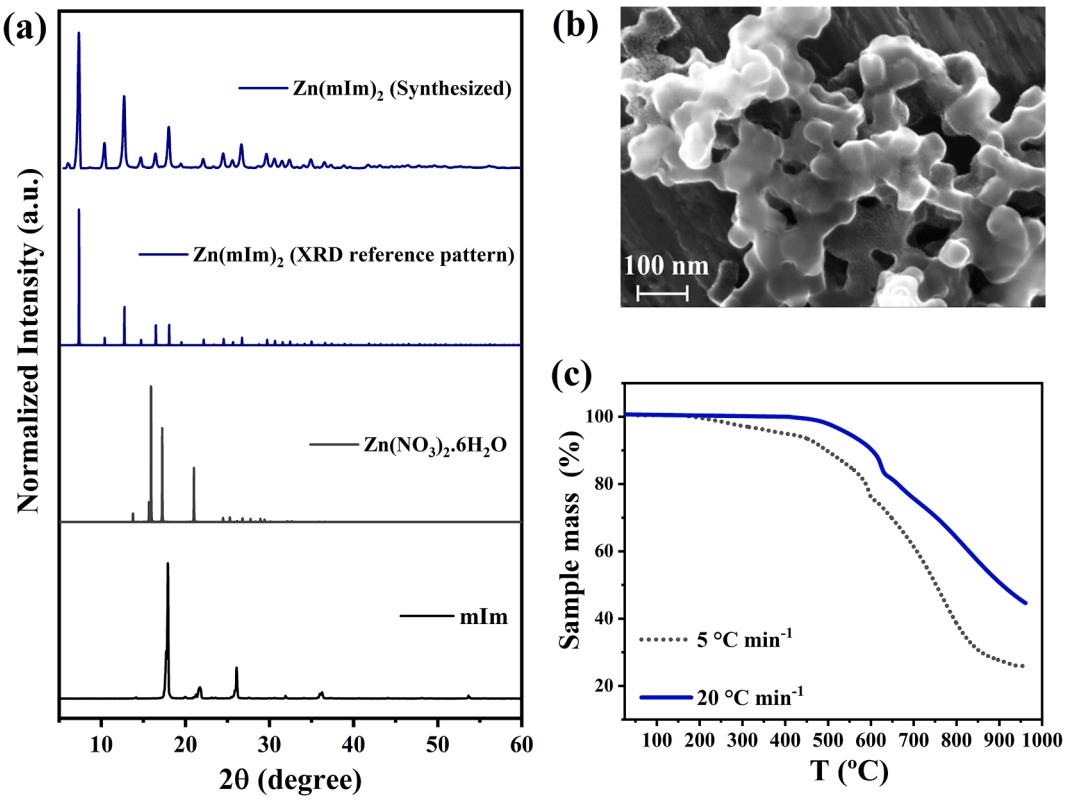

Fig. 1. (a) XRPD patterns for synthesized $Zn(mIm)_2$, a reference pattern from the ICSD database, zinc nitrate hexahydrate, and 2-methylimidazole (mIm). (b) SEM micrograph at a magnification of 300 kX and (c) TG curves under N_2 atmosphere at different heating rate temperature temperatures (5 and 20 °C min^{-1}) for $Zn(mIm)_2$.

C-900, and Fe-N-C-1000.

Fig. 2(a) shows an SEM micrograph of Fe-N-C-700 (as a representative sample of the series), indicating morphology features that result from the combination of the carbon support (Fig. S2(a)) and ZIF-8 (Fig. 1 (b)) morphologies.

Fig. 2(b) shows XRPD patterns of Fe-N-C-700, Fe-N-C-900, and Fe-N-C-1000, indicating the complete carbonization of the $Zn(mIm)_2$ precursor for the three samples, as highlighted by the comparison with the XRPD pattern of the precursors of the Fe-N-C catalysts (Fig. S3).

In addition to the diffraction patterns of graphitic carbon at around 25° and 43°, peaks for iron carbide are observed for the Fe-N-C-700 and Fe-N-C-900 samples, while carbide phases are not evident in the XRPD pattern of Fe-N-C-1000. For the three samples, diffraction peaks for Zn-based phases such as metallic particles and/or oxides were not evidenced.

The XPS survey scans of the samples are reported in Fig. 3(a). Five different core levels are identified, namely C 1s, N 1s, O 1s, Fe 2p, and Zn 2p, originating from the structure of the catalyst. The atomic content of each element is reported in Table 1. Carbon is the predominant element followed by nitrogen and oxygen. Zinc and iron are the less abundant components found in trace within the surface of the catalyst.

The C 1s core levels have been fitted using nine structures, differently than the common literature where seven peaks are usually employed. Indeed, three main C structures were found, C sp^2 located around 284.5 eV, defective C or carbides below 284 eV, and disordered C, of sp^3 hybridization, around 285 eV. In addition, C–N bonds are discriminated from C-O and located at 286 eV, while the oxidized forms of C (C-O, C = O, and C(O)O) can be found at about 287 eV, 288 eV, and 289 eV, respectively (Fig. 3(b)). Nevertheless, the tail of the asymmetric C 1s was found to contain an additional contribution ascribable to plasmon loss features other than the π - π* transitions originating from the aromatic structures [38,59,76–81]. Carbon speciation for Fe-N-C-700, Fe-N-C-900, and Fe-N-C-1000 is reported in Table S2.

Among the samples, at the increase of the pyrolysis temperature, a sensible sharpening of the main region of the C 1s (284–286 eV) is evident due to a decrease in the disordered C structures. In addition, a decrease in the oxidized forms within the spectrum tail is also reported.

In the case of N 1s, the spectra were fitted using seven peaks in the binding energies (BE) range 397–407 eV. Starting from the lower BE, imine or cyano groups (~397.8 eV), pyridinic-N (~398.7 eV), N coordinated to metal (~399.7 eV), pyrrolic-N (~400.7 eV), graphitic- and quaternary-N (401.5 – 402.5 eV), and oxides above 403 eV (Fig. 3(c)) [78,82–90]. The shape of the N 1s becomes wider at the increase of the pyrolysis temperature. The predominant contributions among the samples are the pyridinic moiety, followed by the N coordinated to metal, and pyrrolic nitrogen. In addition, increasing the temperature from 700 to 1000 °C Fe-N_x component increases (Table 2). Overall, the nitrogen content decreased for sample Fe-N-C-1000. For the quantitative evaluation of the moieties' content, refer to Table S2.

Regarding the Fe 2p, a representative fit of its spectrum is reported in Fig. 3(d). As usual with this class of electrocatalysts, the low content of the metal complicates the analysis process. Among the samples, the amount was on average 0.16 at%. The components identified within the Fe 2p spectra are metallic Fe overlapping with carbides (~707 eV), Fe coordinated to nitrogen (~708.4 eV), both Fe oxides in the form of Fe (II) (~709.9 eV) and Fe (III) (~711 eV), and satellite components (>714 eV) [84,86,91–95]. Remarkably, with increasing pyrolysis temperature, the content of metallic Fe overlapping with carbides decreases (Table S2), while the content of coordinated Fe with nitrogen increases (Table 2). Lastly, zinc was found in all samples with a percentage decreasing as the pyrolysis temperature increased, moving from 2% at 700 °C to 0.2% at 1000 °C.

Overall, XPS analysis indicated that the zinc removal is more effective (Table 1) as the pyrolysis temperature increased, and the content of

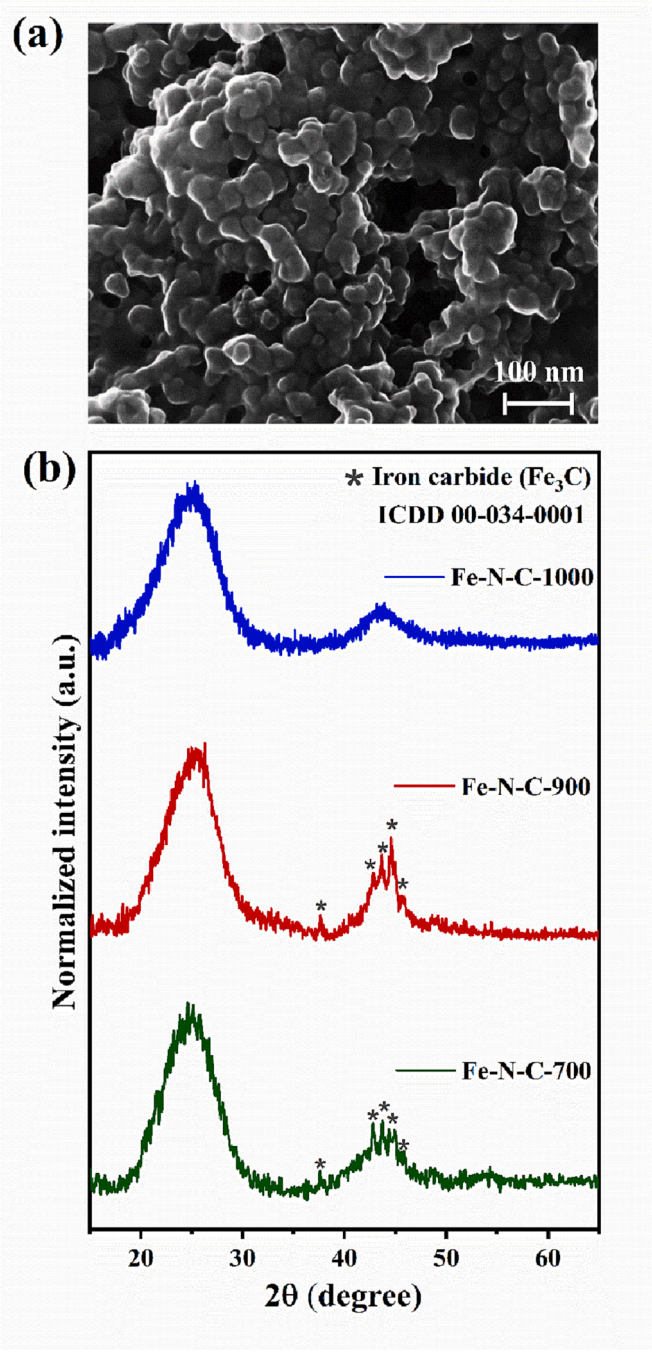

Fig. 2. SEM micrographs at a magnification of 300 kX for Fe-N-C-700 (a) and XRPD patterns for the Fe-N-C-700, Fe-N-C-900, and Fe-N-C-1000 (b).

Fe-N_x-C moieties increased due to the replacement of Zn by iron in the M−N_x−C moieties (Table 2).

Cyclic voltammetry in N_2– and O_2-saturated electrolyte for the three synthesized Fe-N-C catalysts are reported in Fig. 4(a–c). CV in N_2-saturated electrolyte was used for calculating the electrochemical active surface area (ECSA) (Table S3). ECSA decreased with increasing pyrolysis temperature due to the effect of Zn removal in shrinking the carbon matrix ECSA [54,96]. The lower ECSA value was indeed observed for the sample pyrolyzed at 1000 °C (480 $m^2\ g^{-1}$), while ECSA of Fe-N-C-700 and 900 was 665 and 602 $m^2\ g^{-1}$, respectively, in good agreement with ECSA values previously reported for similar M−N−C catalysts [90,97,98]. The CV in O_2-saturated electrolytes showed that all catalysts had a high ORR with a defined reduction peak around 0.8 V (Table S3).

In particular, the activity was higher in peak potential and current density following the trend: Fe-N-C-1000 > Fe-N-C-900 > Fe-N-C-700. The most increased ORR activity of the Fe-N-C-1000 sample can be ascribed to the beneficial effect of the pyrolysis temperature in the zinc removal from the ZIF-based carbon matrix, with the incorporation of nitrogen and iron in more active catalytic sites, despite the reduced ECSA.

ORR activity was further investigated by performing LSV-RRDE experiments. Fig. 4(d) shows I_{ring} and J_{disk} current densities for Fe-N-C-700, Fe-N-C-900, and Fe-N-C-1000 materials at 1600 rpm electrode rotation rate. From J_{disk}, the ORR parameters such as onset (E_{onset}) and half-wave ($E_{1/2}$) potentials and limiting current density (J_{lim}) were extrapolated. The hydrogen peroxide anion (HO_2^-) percentage and the number of electrons exchanged (n) during ORR were calculated using I_{disk} and I_{ring} according to Eqs. S1 and S2.

As can be seen in Fig. 4(d), top panel, no peak signature in the ring current density is observed when potential ranges between 0.8 V and the E_{onset}, characteristic of the O_2 electroreduction on high-active Fe-N_x-C catalytic sites through an electrocatalytic inner-sphere electron transfer (ISET) mechanism [99]. Ring-current peak at around 0.45 V can be ascribed as the oxidation of the hydrogen peroxide anion (HO_2^-) intermediate generated by the carbon matrix at which quinone/hydroquinone functional groups on the carbon edge sites [100] and low-active N-based functional groups mediate O_2 electroreduction *via* an outer-sphere electron transfer (OSET) mechanism (2 × $2e^-$ pathway) [99,101], in good agreement with the slight decrease of n values, when overpotential increases (Table 3). By comparing the Fe-N-C catalysts in terms of the ORR parameters, the Fe-N-C-1000 sample showed the more positive E_{onset} (0.94 V) and $E_{1/2}$ (0.87 V) potentials achieving a high current density value (J_{lim} = -5.66 mA cm^{-2}). Noteworthy, n was kept high at both $E_{1/2}$ (3.99) and 0.2 V (3.92), yielding the lower HO_2^- percentage (0.65 and 3.83 %), indicating that ORR takes place mainly through a direct $4e^-$ transfer pathway.

Tafel plots were also evaluated to get deeper insights into the ORR activity and mechanism of the three prepared catalysts. They were obtained by plotting *i*R-corrected potential values as a function of the logarithm of the kinetic current density, as shown in Fig. 4(e). The plots were linearly fitted in the low current density (*lcd*) region, from *ca* 0.9 to *ca* 0.85 V *vs.* RHE, and in the high current density (*hcd*) region, from *ca* 0.80 V to *ca* 0.75 V *vs.* RHE. From the linear region/*s* in the Tafel plot, which corresponds to a Tafel behavior, exchange current density (J_0) and the cathodic transfer coefficient (α_c) were calculated after the determination of the slope ($2.303RT/\alpha_cF$) and the intercept (E^0 + ($2.303RT/\alpha_cF$) log(J_0)) respectively, according to Eq. S4 [102,103]. The calculated parameters from the Tafel analysis for the Fe-N-C samples are reported in Table S4.

For all samples, Tafel slopes are around 60 mV dec^{-1} (in the *lcd* region) and in the range of 100 to 120 mV dec^{-1} (in the *hcd* region), in good agreement with Tafel slope values reported in the literature for Pt/C [104,105]. This finding indicates that ORR at the electrode surface of three samples follows a similar mechanism with a rate-determining step (*rds*) characterized by a second electron transfer and splitting of the O-O bond [106–108]. Despite a similar mechanism, exchange current density (J_0) in both *lcd* and *hcd* regions corroborates the activity trend (Fe-N-C-1000 > Fe-N-C-900 > Fe-N-C-700) observed in the previous electrochemical analysis.

3.1. Accelerated stress tests (ASTs)

For elucidating material performance in terms of durability, two different accelerated stress tests (AST) were carried out (Fig. S4): the ECSA retention and the load-cycle test, to evaluate ECSA, and ORR parameters change over time, respectively, as a consequence of both carbon matrix and active site degradation [64]. Experiments were performed over 30,000 cycles in N_2-saturated electrolyte and ORR activity accessed by LSV-RDE experiments under O_2-saturated electrolyte.

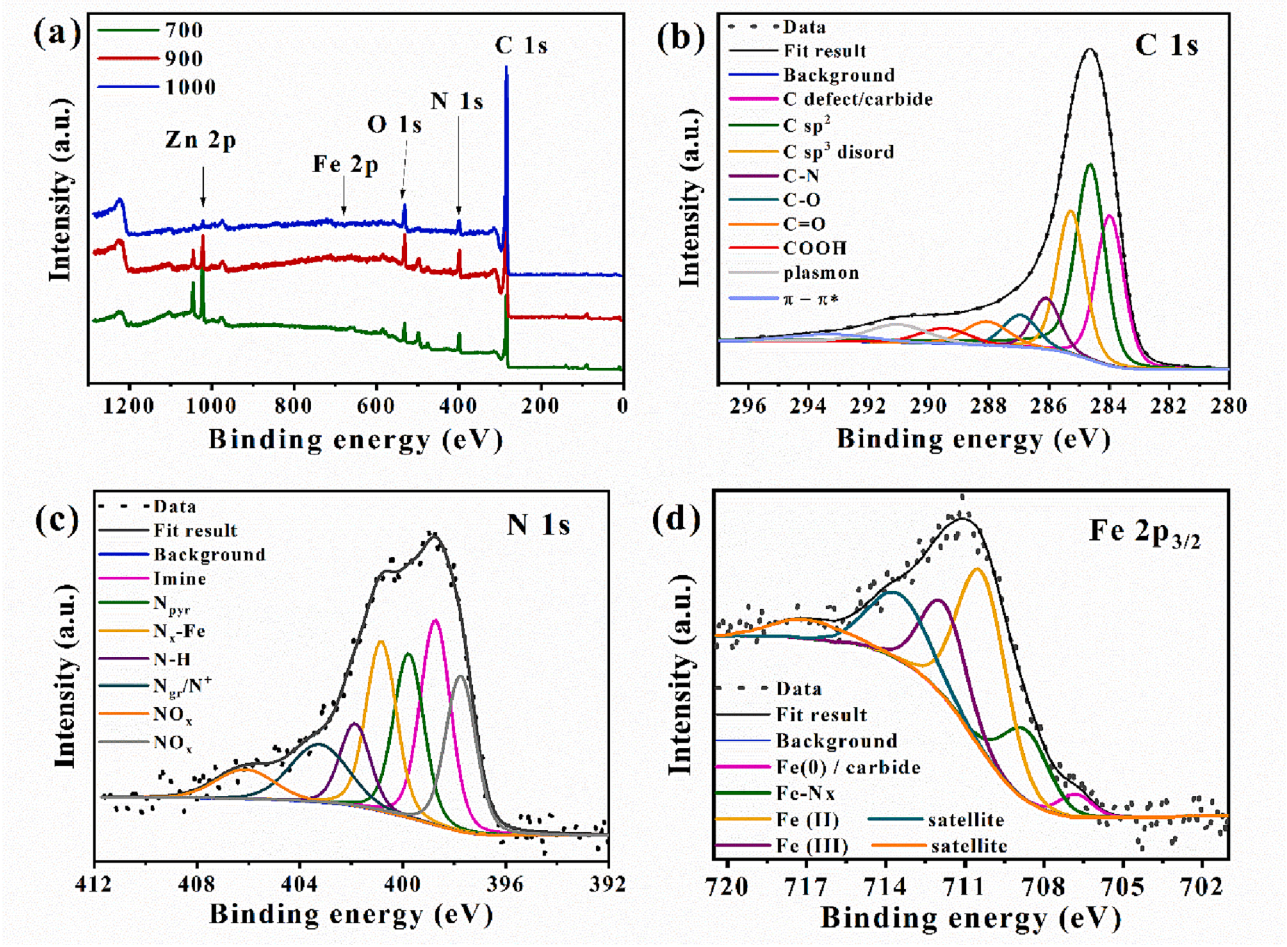

Fig. 3. Survey scans of Fe-N-C-700, Fe-N-C-900, and Fe-N-C-1000 samples (a) and C 1s (b), N 1s (c), and and Fe 2p centered on the $2p_{3/2}$ component (d) of the representative Fe-N-C-1000 sample.

Table 1
Elemental composition obtained by XPS analysis of the three synthesized catalysts.

Sample	C (At. %)	N (At. %)	O (At. %)	Zn (At. %)	Fe (At. %)
Fe-N-C-700	87.08	7.51	3.28	1.97	0.15
Fe-N-C-900	85.93	7.76	5.28	0.80	0.22
Fe-N-C-1000	89.80	5.33	4.54	0.20	0.12

Table 2
$M-N_x$ and $Fe-N_x$ relative content obtained by the chemical speciation of the N 1s and Fe $2p_{3/2}$ XPS spectra, respectively.

Sample	$M-N_x$ (N 1s)		$Fe-N_x$ (Fe $2p_{3/2}$)	
	BE (eV)	Content (Rel. %)	BE (eV)	Content (Rel. %)
Fe-N-C-700	399.7	16.7	708.5	4.3
Fe-N-C-900	399.8	17.9	708.6	6.5
Fe-N-C-1000	399.8	17.5	708.7	19.5

Fig. 5(a, b) shows the ECSA retention for Fe-N-C-1000 compared with that of Pt/C estimated from the CVs recorded in static conditions. A high ECSA retention (94 %) was observed for the Fe-N-C-1000 catalyst over 30,000 CV cycles, with the main drops found over the first 10.000 cycles. Differently, the Pt/C electrode showed a progressive ECSA decrease with a 35 % retention at the end of the test. Indeed, the CV profile for Fe-N-C-1000 before and after the AST (inset of Fig. 5(a)) was almost the same. By contrast, for Pt/C (inset of Fig. 5(b)), not only did hydrogen-underpotential deposition (H_{UPD}) significantly decrease, leading to a significant ECSA loss but also the profile of PtO formation and reduction regions changed. The huge flattening in the H_{UPD} region and changes in the PtO formation and reduction regions are in agreement with previous studies demonstrating that the considerable decrease in the Pt/C electrode durability during AST is mainly related to carbon support corrosion and the detachment of the supported Pt nanoparticles (NPs) [109]. According to Lafforgue et al. [63], PGM-based (e.g., Ru, Pt, and Pd) particles promote carbon support corrosion into CO_2, leading to the local production of solid carbonates, destroying the anchoring sites between the PGM-based NPs and the carbon support. The intermediates of carbon oxidation interact with the Pt nanoparticles to create $Pt\text{-}CO_{ads}$ species ($Pt + C_n\text{-}CO_{ads} \rightarrow Pt\text{-}CO_{ads} + C_n$); at potential values higher than 0.6 V *vs.* RHE, CO_{ads} reacts with OH_{ads} and OH^- species to form CO_2 ($Pt\text{-}CO_{ads} + Pt\text{-}OH_{ads} + OH^- \rightarrow CO_2 + H_2O + 2Pt$), which converts into alkali-metal carbonates ($CO_2 + 2OH^- \rightarrow CO_3^{2-} + H_2O$) such as K_2CO_3, considering an electrolyte solution based on KOH.

LSV-RRDE curves (Fig. 5(c) and 5(d)) recorded before and after the load-cycle tests showed that onset and half-wave potentials slightly shift toward lower values and the limiting current density slightly decrease. Those minor changes in ORR parameters after cycling are comparable and even lower than those observed for other PGM-free catalysts tested in similar conditions [110,111], indicating good durability of Fe-N-C-1000. By contrast, the state-of-the-art Pt/C exhibits much more significant changes in ORR parameters, resulting in a 95% mass activity decrease at 0.9 V *vs.* RHE for Pt/C *vs.* 46% for Fe-N-C-1000 (Table S5).

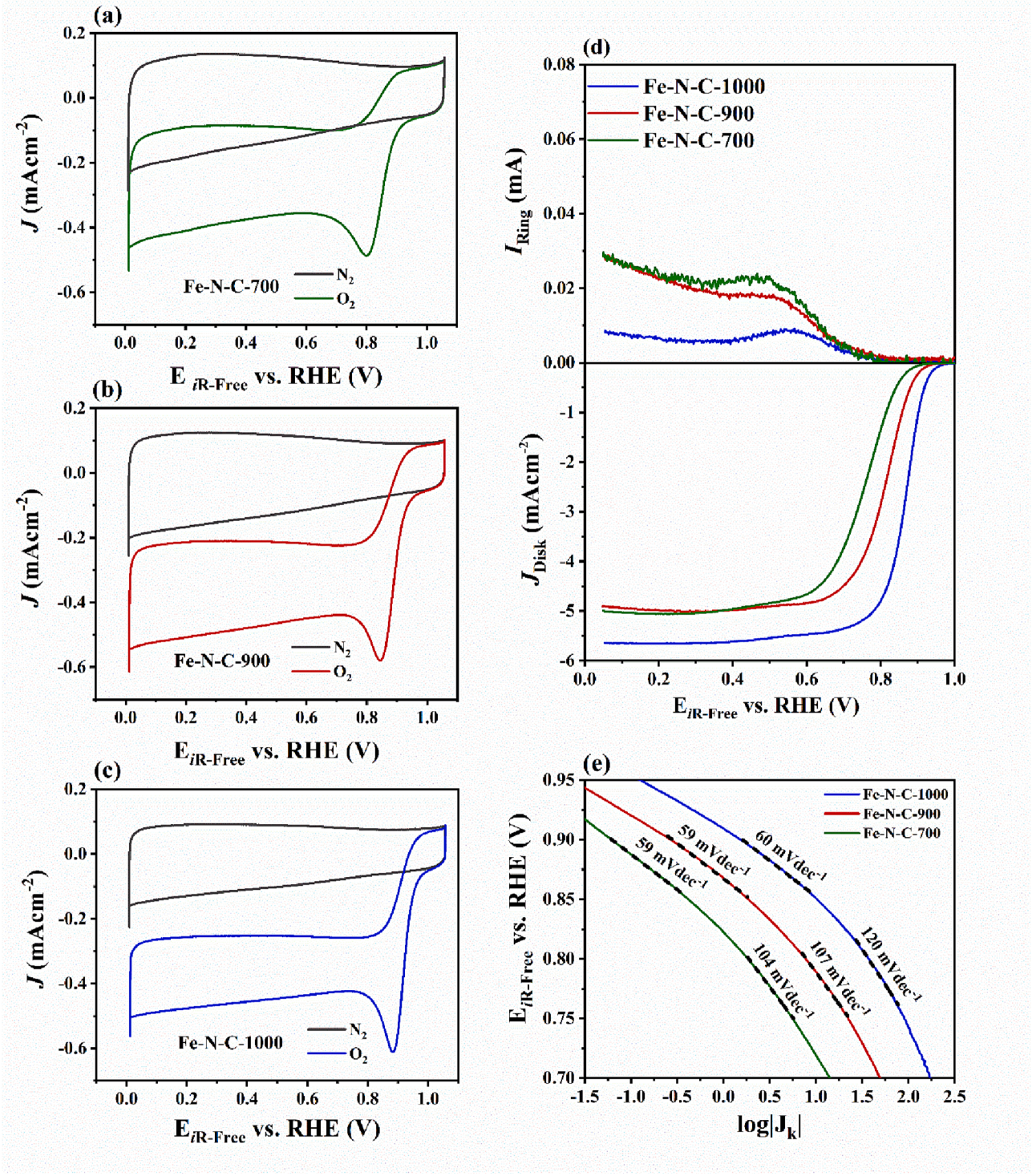

Fig. 4. CV (5 mV s^{-1} scan rate) in N_2– and O_2-saturated KOH (0.1 M) electrolyte for the catalysts obtained at 700 (a), 900 (b), and 1000 °C (c). LSV-RRDE experiments at a scan rate of 5 mV s^{-1} and rotation speed of 1600 rpm: ring current (top panel) and disk (bottom panel) current density (d) and Tafel plots for the Fe-N-C catalysts (e).

Both accelerated stress tests indicated that the MOF precursor combined with the carbon black pearls used as conductive support were effective in obtaining high-active and stable catalytic sites towards ORR. The optimized Fe-N-C-1000 catalyst demonstrated high performance in simulated AEMFC operating conditions.

3.2. Methanol tolerance

To evaluate the applicability of the Fe-N-C-1000 catalyst at the cathode of an ADMFC, performance durability tests were performed by simulating the methanol crossover effect on the ORR activity. LSV curves and EIS spectra were acquired using an RDE set-up in a half-cell configuration. Fig. 6(a, b) show LSV curves recorded at different methanol concentrations (0.01, 0.05, 0.1, 0.5, 1.0, and 2.0 M) for Fe-N-

Table 3
Onset potential (E_{onset}), half-wave potential ($E_{1/2}$), limiting current density (J_{lim}), number of electrons transferred (n), and peroxide percentage (HO_2^- %) for Fe-N-C catalysts at a scan rate of 5 mV s^{-1} and rotation speed of 1600 rpm.

Sample	Onset potential (E_{onset})	Half-wave potential ($E_{½}$)	J_{lim}	Number of electrons transferred (n)		HO_2^- (%)	
	E *vs.* RHE (V)	E *vs.* RHE (V)	($mAcm^{-2}$) at 0.2 V	$E = E_{½}$	E *vs.* RHE = 0.2 V	$E = E_{½}$	E *vs.* RHE = 0.2 V
Fe-N-C-700	0.87 ± 0.01	0.76 ± 0.01	−5.06 ± 0.01	3.94 ± 0.03	3.64 ± 0.03	2.9 ± 1.2	17.6 ± 1.6
Fe-N-C-900	0.91 ± 0.01	0.81 ± 0.01	−4.93 ± 0.10	3.97 ± 0.01	3.65 ± 0.04	1.5 ± 0.2	17.6 ± 2.0
Fe-N-C-1000	0.94 ± 0.01	0.87 ± 0.01	−5.66 ± 0.01	3.99 ± 0.01	3.92 ± 0.02	0.65 ± 0.04	3.8 ± 1.0

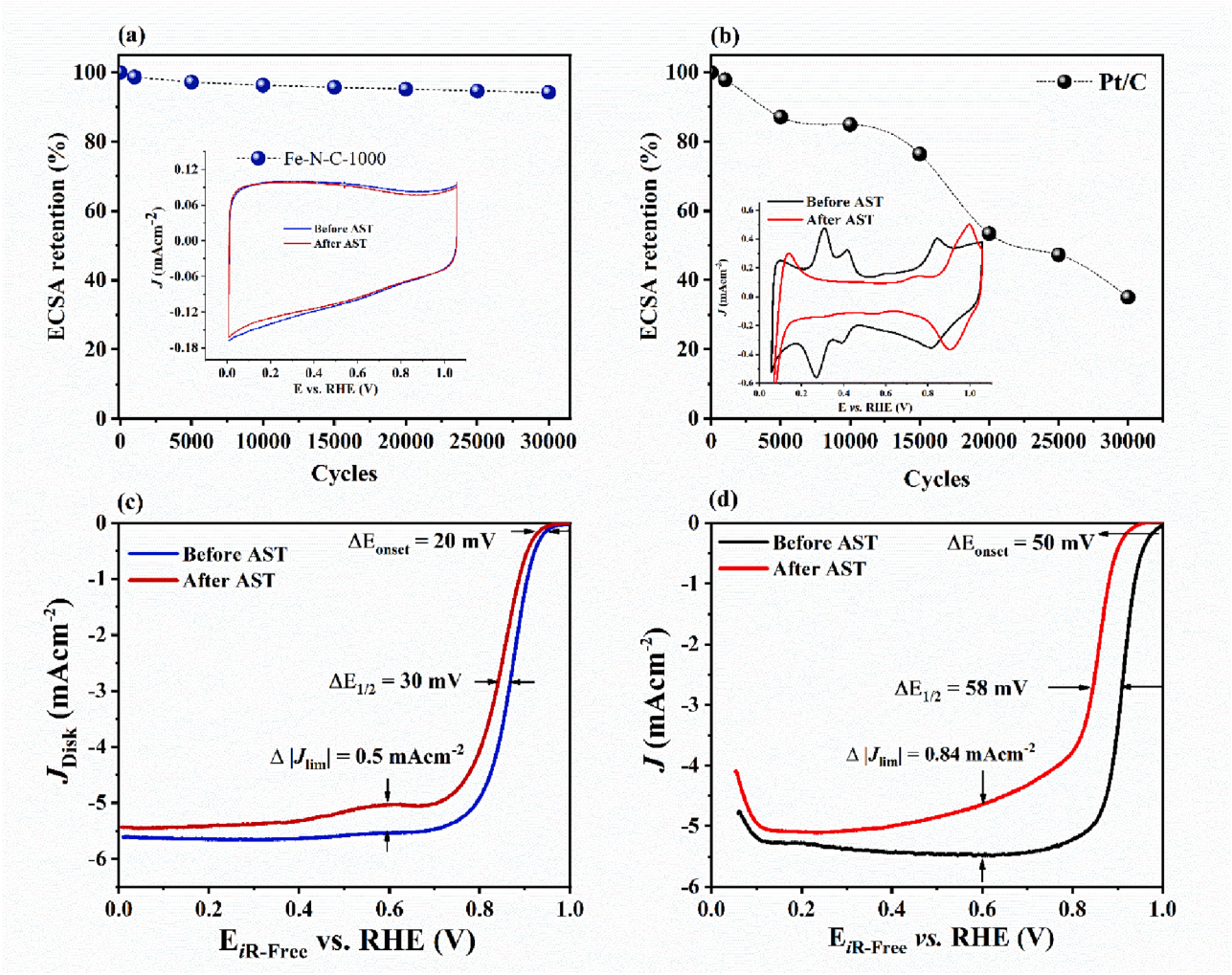

Fig. 5. ECSA retention over the durability tests estimated from CV in N_2– saturated 0.1 M KOH at 5 and 50 mV s^{-1} potential scan rate (Inset of the figure) for Fe-N-C-1000 (0.20 mg cm^{-2} loading) (a) and Pt/C (16 μgcm^{-2} Pt-loading) (b) electrodes. Disk current densities obtained from LSV-RDE experiments at a scan rate of 5 mV s^{-1} and rotation speed of 1600 rpm before and after the load-cycle AST for Fe-N-C-1000 (c) and Pt/C (d).

C-1000 and Pt/C, respectively. ORR parameters (E_{onset}, $E_{1/2}$, and J_{lim}) remained almost constant for the Fe-N-C-1000 sample up to a 2 M CH_3OH concentration. At the same time, for Pt/C the methanol oxidation reaction took place even at low methanol concentrations (0.05 M), affecting ORR parameters [11]. These results indicate higher methanol tolerance of the active sites in the Fe-N-C material compared to state-of-the-art Pt/C active sites.

To deepen on methanol tolerance features of Fe-N-C-1000, the impedance spectra of Fe-N-C-1000 and Pt/C electrode were recorded under hydrodynamic conditions in fresh O_2-saturated electrolyte, and methanol-containing electrolyte (Fig. 6(c–f)). Different equivalent circuit (EC) elements were used to model the processes at the surface of both catalysts, a single Randles-type circuit for Fe-N-C-1000 and an in-series distributed circuit for Pt/C. In the EC (inset of Fig. 6(c) and 6 (d)), R_s represents the solution resistance, and the arc/semi-circle is represented by a polarization resistance (R_p) across the electrode–electrolyte interface, which is governed by the charge-transfer resistance (R_{p1}) at high potentials and mass-transfer resistance (R_{p2}) at low potentials. The constant phase element (Q_1 and Q_2) is related to double-layer capacitance [112]. According to previous studies, the contribution of impedance from R_{p1} and R_{p2} is minimum at the mixed kinetic + diffusion region [112,113]; for this reason, EIS spectra were recorded at the half-wave zone of the polarization curve to evaluate the methanol effect on the impedance.

The resistance values obtained from data fit are reported in Table S6. For the Fe-N-C-1000 electrode, solution resistance in the fresh

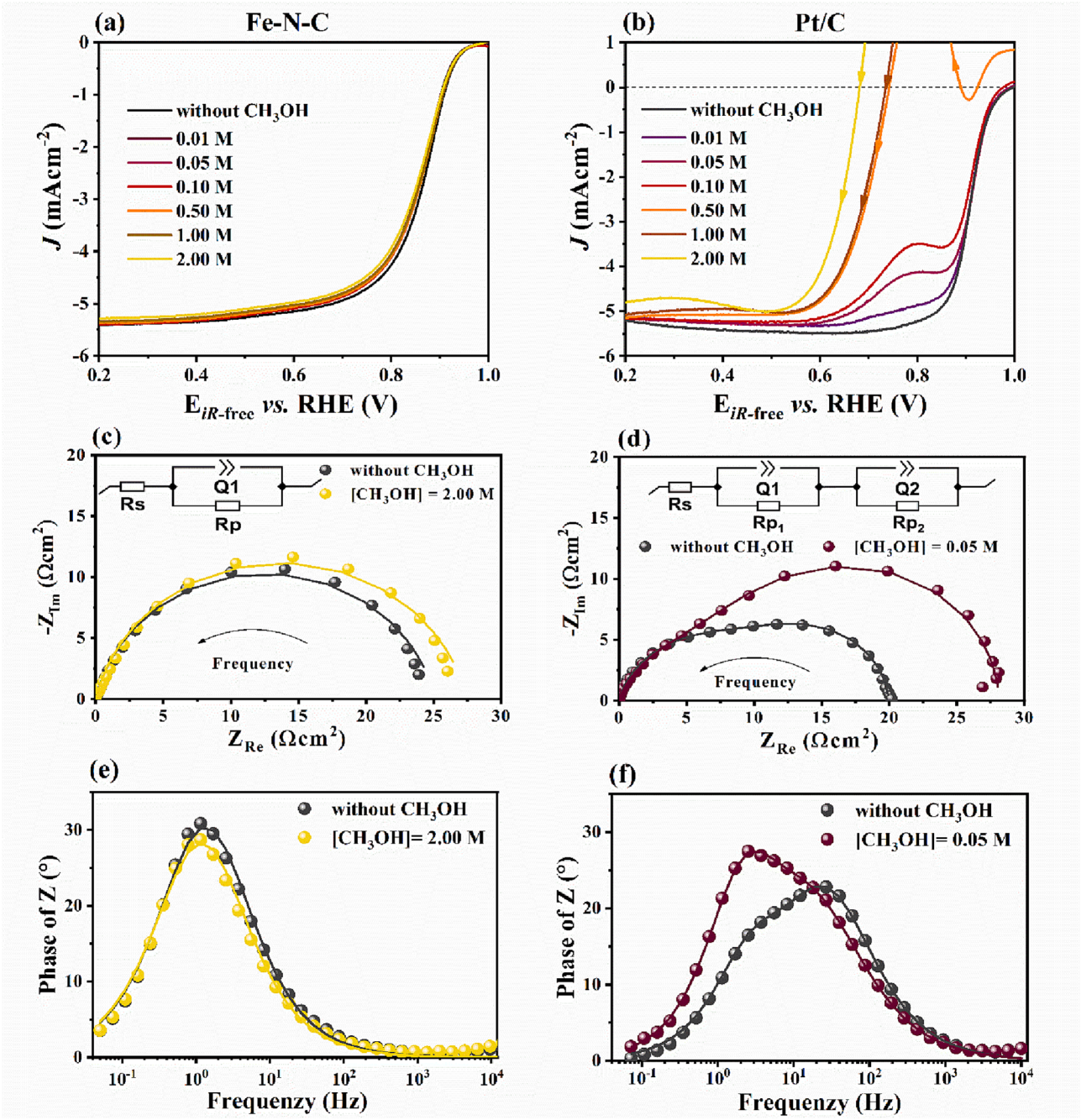

Fig. 6. LSV-RDE experiments and EIS spectra were acquired at the electrode rotation speed of 1600 rpm in 0.1 M KOH for the Fe-N-C-1000 sample (a), and Pt/C taken as control (b). Nyquist plots at the half-wave potential of both Fe-N-C-1000 (c) and Pt/C (d) catalysts, with and without adding 2.00 M and 0.05 M CH_3OH, respectively. Bode plots of Fe-N-C-1000 (e) and Pt/C (f) catalysts, with and without adding 2.00 M and 0.05 M CH_3OH, respectively.

electrolyte was 8.5 Ω cm^2 and reached 10.5 Ω cm^2 at a 2 M methanol concentration. In comparison, for the Pt/C electrode, it was almost constant (7.4 ± 0.1 Ω cm^2) since impedance data were recorded at a lower methanol concentration (0.05 M). Those values were subtracted from the impedance data in the Nyquist plots as shown in Fig. 6(c) and 6 (d).

Nyquist plots for both electrodes with and without methanol had different profiles. For Fe-N-C-1000, the contribution of R_{p1} and R_{p2} are not distinguishable at the mixed kinetic-diffusion controlled region, and the polarization resistance is characterized by a single semi-circle at high-frequencies (HF) as indicated by the Bode plot (Fig. 6(e)). However, for the Pt/C electrode, two semi-circles are observed at low-frequency (LF) and HF, minor and higher shoulder in the Bode plot (Fig. 6(f), without methanol), respectively. The R_{p1}, Q_1 elements are due to the charge-transfer process through the electrode–electrolyte interface, and the R_{p2}, Q_2 elements are due to O_2 mass transport [112].

By comparing the effect of methanol on the EIS spectra, polarization resistance ($R_{p1} + R_{p2}$) for the Fe-N-C catalyst increased by 9.2% at a 2 M methanol concentration. Noteworthy, $R_{p1} + R_{p2}$ was higher for the Pt/C (41.5%) at a lower methanol concentration (0.05 M), in good agreement with the shift of the ORR polarization curves toward lower potential values. These results demonstrate the higher methanol tolerance of the active sites in the Fe-N-C catalyst compared to Pt/C.

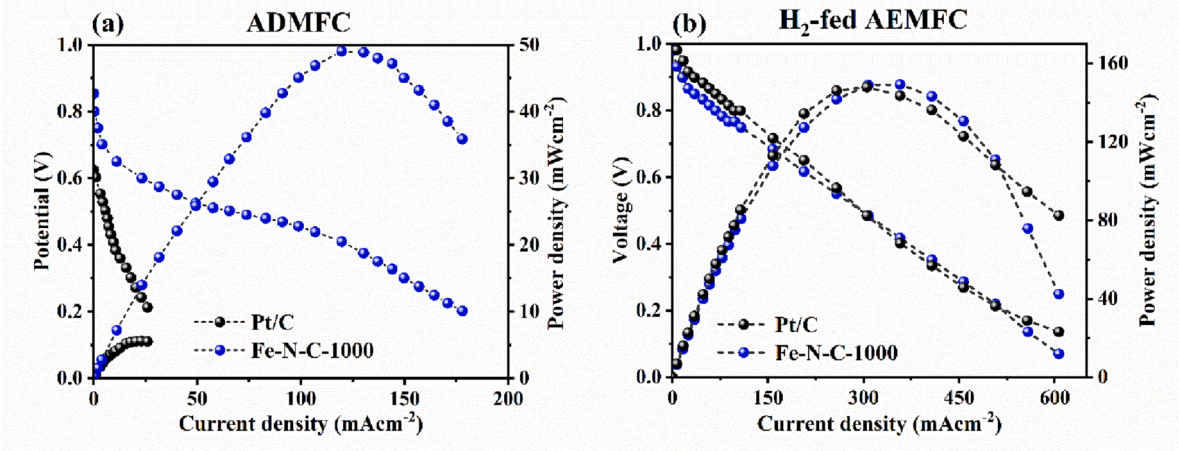

Fig. 7. Polarization and power density curves for Fe-N-C and Pt/C-based MEAs at 60 °C for an ADMFC fed with 1 M KOH / 5 M CH_3OH (a) and an AEMFC fed with H_2 (1.0 bar abs, 100% RH) (b).

Table 4
Electrochemical parameters for the tested MEAs assembled with the Fe-N-C-1000 (4.5 mgcm^{-2}) and Pt/C (0.5 mgcm^{-2} Pt loading) as cathode electrocatalyst of the H_2-fed AEMFC.

Cathode electrocatalyst and loading (mgcm^{-2})	OCV (V)	R_{cell}, (Ωcm^2)	E_{cell} @ 200 mAcm^{-2} (mV)	J @ 0.6 V (mAcm^{-2})	J_{Max} (mAcm^{-2})	Maximum power density (mWcm^{-2})
Fe-N-C-1000	0.98	0.25	617	207	606	149
Pt/C	1.05	0.27	650	257	600	148

3.3. AEMFC and ADMFC tests

Given the high methanol tolerance, the Fe-N-C-1000 electrocatalyst was assembled at the cathode side of an ADMFC prototype. Fig. 7(a) shows polarization and power density curves recorded at 60 °C feeding the anode with a 5 M methanol solution and the cathode with oxygen. MEAs based on commercial Pt/C were also investigated and taken as control. The highest performance for the cell operating with the Fe-N-C catalyst at cathode side was obtained at 60 °C (Fig. S5), and reached a maximum power density of 49 mW cm^{-2} (normalized performance with respect to Pt loading = 32.7 mW mg_{Pt}), which is significantly higher than that achieved for the cell assembled with Pt/C cathode-based MEA (5.6 mW cm^{-2}), as shown in Fig. 7(a). The superior performance of the Fe-N-C cathode-based MEA can be ascribed to the high tolerance of the catalyst active sites to methanol crossover as compared to Pt/C, as pointed out by methanol tolerance studies. This feature was further confirmed by analyzing the effect of different methanol concentrations (1, 2, 5, 10 M) on cell performance at 60 °C (Fig. S6). The maximum power density was reached at 5 M CH_3OH (in 1 M KOH). It slightly decreased feeding 10 M methanol solution, maintaining the open circuit voltage (OCV) almost unvaried, as proof of the extraordinary tolerance of such a catalyst to methanol poisoning.

Fuel cell performance investigation was deepened by assembling the material at the cathode side of an AEMFC fed with H_2 at the anode. Fig. 7 (b) shows the I-V and power density curves obtained at 60 °C with the MEA based on the Fe-N-C-1000 cathode and a Pt/C cathode taken as control. The extrapolated parameters are reported in Table 4, indicating high open-circuit voltage and maximum power density, which were competitive with the state-of-the-art Pt/C electrode.

Comparing the fuel cell performance obtained assembling previously reported M−N−C catalysts at the cathode side and using a FUMASEP® FAA-3-50 membrane, the Fe-N-C-1000 material had similar or even higher maximum peak power density values, in ADMFC [114,115] and H_2-fed AEMFC [116–121] Noteworthily, both the performance achieved in ADMFC and H_2-fed AEMFC in this work, outperformed the performance achieved by commercial Fe-N-C catalysts manufactured by Pajarito Powder [122]. Table S7 and S8 reports a comparison of maximum power density values obtained with different PGM-free catalysts assembled at the cathode side of ADMFC and H_2-fed AEMFC, respectively, equipped with FUMASEP and other anion exchange membranes [123–130].

4. Conclusions

This study demonstrated the effect of tailored pyrolysis conditions to boost ORR activity of ZIF-derived Fe-N-C catalysts in an alkaline environment, as pointed out by high onset and half-wave potentials, limiting current density values, with ORR mostly taking place through a 4e$^-$ transfer pathway. The Tafel analysis indicated that ORR proceeds through the same rating-determining mechanism at the surface of the three catalysts independently on the pyrolysis temperature; by contrast, the exchange current densities values were higher for the sample pyrolyzed at 1000 °C, indicating the higher density of active sites with the replacement of Zn from the ZIF-8 structure by more active Fe-based functional groups, as confirmed by XPS analysis. In addition to the high activity, accelerated stress tests over 30,000 cycles also indicated high-performance durability for the optimized Fe-N-C-1000 catalyst compared to Pt/C, with only minor variations in ECSA, E_{onset}, $E_{1/2}$, and J_{lim} over cycling. The Fe-N-C active sites also demonstrated good stability in the presence of methanol, pointing at an enhanced methanol tolerance compared to Pt/C.

The high ORR activity and methanol tolerance were reflected in the results obtained assembling Fe-N-C-1000 in either ADMFC or H_2-fed AEMFC equipped with a low-cost commercial FUMASEP® FAA-3-50 membrane. Regarding ADMFC performance, the best results were achieved by feeding the anode with a 5 M methanol solution and 60 °C operating temperature. Those conditions enhanced the kinetics of methanol oxidation and oxygen reduction as well as membrane conductivity. An exceptionally high-power density (49 mW cm^{-2}) was recorded in ADMFC due to the high tolerance to methanol of the Fe–N–C electrocatalyst. This is one of the highest performances reached for a MEA based on the low-cost FAA-3-50 commercial membrane and a

PGM-free cathode. Moreover, a very high-power density was achieved (149 mW cm^{-2}) also in H_2-fed AEMFC, indicating that tailored pyrolysis conditions and iron decoration on the MOF template were effective to guarantee high energy output in the AEMFC. The high activity and exceptional methanol tolerance of the MOF-derived Fe-N_x active sites under operating conditions place Fe-N-C-1000 as a promising and cost-effective candidate to replace Pt/C at the cathode of both ADMFC and AEMFC devices.

Declaration of Competing Interest

The authors declare the following financial interests/personal relationships which may be considered as potential competing interests: ALESSANDRA D'EPIFANIO, BARBARA MECHERI, ERNESTO PLACIDI report financial support was provided by Lazio Region.

Data availability

Data will be made available on request.

Acknowledgments

This work has received funding from the Regione Lazio through the project POR FESR LAZIO 2014–2020, N∘ A0375-2020-36492. VCAF is grateful to "Avvio alla ricerca funding" from Sapienza University of Rome.

The integrated XPS were carried out at the SmartLab departmental laboratory of the Department of Physics at Sapienza University of Rome. EP and VCAF are grateful to Dr. M. Sbroscia for his assistance during the measurements.

Appendix A. Supplementary data

Supplementary data to this article can be found online at https://doi.org/10.1016/j.cej.2023.142987.

References

[1] N. Ramaswamy, S. Mukerjee, Alkaline anion-exchange membrane fuel cells: challenges in electrocatalysis and interfacial charge transfer, Chem. Rev. 119 (2019) 11945–11979, https://doi.org/10.1021/acs.chemrev.9b00157.
[2] N. Ul Hassan, M. Mandal, G. Huang, H.A. Firouzjaie, P.A. Kohl, W.E. Mustain, Achieving high-performance and 2000 h stability in anion exchange membrane fuel cells by manipulating ionomer properties and electrode optimization, Adv. Energy Mater. 10 (2020) 1–8, https://doi.org/10.1002/aenm.202001986.
[3] M.M. Hossen, M.S. Hasan, M.R.I. Sardar, J.B. Haider, Mottakin, K. Tammeveski, P. Atanassov, State-of-the-art and developmental trends in platinum group metal-free cathode catalyst for anion exchange membrane fuel cell (AEMFC), Appl. Catal. B Environ. 325 (2023) 121733.
[4] G. Liu, A. Wang, W. Ji, F. Zhang, J. Wu, T. Zhang, H. Tang, H. Zhang, In-situ crosslinked, side chain polybenzimidazole-based anion exchange membranes for alkaline direct methanol fuel cells, Chem. Eng. J. 454 (2023), 140046, https://doi.org/10.1016/J.CEJ.2022.140046.
[5] V. Antonucci, V. Baglio, A.S. Aricò, Direct methanol fuel cells: history, status and perspectives, John Wiley and Sons (2009), https://doi.org/10.1002/9783527627707.
[6] D. Shi, L. Cai, C. Zhang, D. Chen, Z. Pan, Z. Kang, Y. Liu, J. Zhang, Fabrication methods, structure design and durability analysis of advanced sealing materials in proton exchange membrane fuel cells, Chem. Eng. J. 454 (2023), 139995, https://doi.org/10.1016/J.CEJ.2022.139995.
[7] G.C. Abuin, E.A. Franceschini, P. Nonjola, M.K. Mathe, M. Modibedi, H.R. Corti, A high selectivity quaternized polysulfone membrane for alkaline direct methanol fuel cells, J. Power Sources. 279 (2015) 450–459, https://doi.org/10.1016/j.jpowsour.2014.12.136.
[8] W.E. Mustain, Understanding how high-performance anion exchange membrane fuel cells were achieved: component, interfacial, and cell-level factors, Curr. Opin. Electrochem. 12 (2018) 233–239, https://doi.org/10.1016/J.COELEC.2018.11.010.
[9] X. Li, Y. Huang, Z. Chen, S. Hu, J. Zhu, P. Tsiakaras, P. Kang Shen, Novel PtNi nanoflowers regulated by a third element (Rh, Ru, Pd) as efficient multifunctional electrocatalysts for ORR, MOR and HER, Chem. Eng. J. 454 (2023), 140131, https://doi.org/10.1016/J.CEJ.2022.140131.
[10] Z. Chen, C. Hao, B. Yan, Q. Chen, H. Feng, X. Mao, J. Cen, Z.Q. Tian, P. Tsiakaras, P.K. Shen, ZIF-Mg(OH)2 dual template assisted self-confinement of small ptco nps as promising oxygen reduction reaction in pem fuel cell, Adv. Energy Mater. 12 (2022) 2201600, https://doi.org/10.1002/aenm.202201600.
[11] D. Sebastián, A. Serov, I. Matanovic, K. Artyushkova, P. Atanassov, A.S. Aricò, V. Baglio, Insights on the extraordinary tolerance to alcohols of Fe-N-C cathode catalysts in highly performing direct alcohol fuel cells, Nano Energy. 34 (2017) 195–204, https://doi.org/10.1016/j.nanoen.2017.02.039.
[12] C. Lo Vecchio, A. Serov, M. Dicome, B. Zulevi, A.S. Aricò, V. Baglio, Investigating the durability of a direct methanol fuel cell equipped with commercial platinum group metal-free cathodic electro-catalysts, Electrochim. Acta. 394 (2021), 139108, https://doi.org/10.1016/j.electacta.2021.139108.
[13] V. Baglio, A. Stassi, O. Barbera, G. Giacoppo, D. Sebastian, C. D'Urso, M. Schuster, B. Bauer, J.L. Bonde, A.S. Aricò, Direct methanol fuel cell stack for auxiliary power units applications based on fumapem® F-1850 membrane, Int. J. Hydrogen Energy. 42 (2017) 26889–26896, https://doi.org/10.1016/j.ijhydene.2017.08.109.
[14] C. Lo Vecchio, A. Serov, H. Romero, A. Lubers, B. Zulevi, A.S. Aricò, V. Baglio, Commercial platinum group metal-free cathodic electrocatalysts for highly performed direct methanol fuel cell applications, J. Power Sources. 437 (2019) 226948.
[15] L. Osmieri, J. Park, D.A. Cullen, P. Zelenay, D.J. Myers, K.C. Neyerlin, Status and challenges for the application of platinum group metal-free catalysts in proton-exchange membrane fuel cells, Curr. Opin. Electrochem. 25 (2021), 100627, https://doi.org/10.1016/J.COELEC.2020.08.009.
[16] M. Luis-Sunga, J.L. Rodríguez, G. García, E. Pastor, Oxygen electroreduction reaction at bidimensional materials, Curr. Opin. Electrochem. 23 (2020) 139–144, https://doi.org/10.1016/J.COELEC.2020.05.015.
[17] S. Akula, M. Mooste, J. Kozlova, M. Käärik, A. Treshchalov, A. Kikas, V. Kisand, J. Aruväli, P. Paiste, A. Tamm, J. Leis, K. Tammeveski, Transition metal (Fe Co, Mn, Cu) containing nitrogen-doped porous carbon as efficient oxygen reduction electrocatalysts for anion exchange membrane fuel cells, Chem. Eng. J. 458 (2023), 141468, https://doi.org/10.1016/J.CEJ.2023.141468.
[18] S. Specchia, P. Atanassov, J.H. Zagal, Mapping transition metal–nitrogen–carbon catalyst performance on the critical descriptor diagram, Curr. Opin. Electrochem. 27 (2021), 100687, https://doi.org/10.1016/j.coelec.2021.100687.
[19] J. Lilloja, M. Mooste, E. Kibena-Põldsepp, A. Sarapuu, A. Kikas, V. Kisand, M. Käärik, J. Kozlova, A. Treshchalov, P. Paiste, J. Aruväli, J. Leis, A. Tamm, S. Holdcroft, K. Tammeveski, Cobalt-, iron- and nitrogen-containing ordered mesoporous carbon-based catalysts for anion-exchange membrane fuel cell cathode, Electrochim. Acta. 439 (2023), 141676, https://doi.org/10.1016/J.ELECTACTA.2022.141676.
[20] S.S.A. Shah, T. Najam, M.S. Javed, M.M. Rahman, P. Tsiakaras, Novel Mn-/Co-Nx moieties captured in n-doped carbon nanotubes for enhanced oxygen reduction activity and stability in acidic and alkaline media, ACS Appl. Mater. & Interfaces. 13 (19) (2021) 23191–23200.
[21] M.A. Costa de Oliveira, B. Mecheri, A. D'Epifanio, E. Placidi, F. Arciprete, F. Valentini, A. Perandini, V. Valentini, S. Licoccia, Graphene oxide nanoplatforms to enhance catalytic performance of iron phthalocyanine for oxygen reduction reaction in bioelectrochemical systems, J. Power Sources. 356 (2017) 381–388, https://doi.org/10.1016/j.jpowsour.2017.02.009.
[22] F. Shahbazi Farahani, B. Mecheri, M. Reza Majidi, M.A. Costa de Oliveira, A. D'Epifanio, F. Zurlo, E. Placidi, F. Arciprete, S. Licoccia, MnOx-based electrocatalysts for enhanced oxygen reduction in microbial fuel cell air cathodes, J. Power Sources. 390 (2018) 45–53, https://doi.org/10.1016/j.jpowsour.2018.04.030.
[23] F. Shahbazi Farahani, B. Mecheri, M.R. Majidi, E. Placidi, A. D'Epifanio, Carbon-supported Fe/Mn-based perovskite-type oxides boost oxygen reduction in bioelectrochemical systems, Carbon N. Y. 145 (2019) 716–724, https://doi.org/10.1016/j.carbon.2019.01.083.
[24] C. Santoro, R. Gokhale, B. Mecheri, A. D'Epifanio, S. Licoccia, A. Serov, K. Artyushkova, P. Atanassov, Design of Iron(II) phthalocyanine-derived oxygen reduction electrocatalysts for high-power-density microbial fuel cells, ChemSusChem. 10 (2017) 3243–3251, https://doi.org/10.1002/cssc.201700851.
[25] G. Lemes, D. Sebastián, E. Pastor, M.J. Lázaro, N-doped graphene catalysts with high nitrogen concentration for the oxygen reduction reaction, J. Power Sources. 438 (2019), 227036, https://doi.org/10.1016/J.JPOWSOUR.2019.227036.
[26] S. Pérez-Rodríguez, D. Sebastián, C. Alegre, T. Tsoncheva, N. Petrov, D. Paneva, M.J. Lázaro, Biomass waste-derived nitrogen and iron co-doped nanoporous carbons as electrocatalysts for the oxygen reduction reaction, Electrochim. Acta. 387 (2021), 138490, https://doi.org/10.1016/J.ELECTACTA.2021.138490.
[27] J.M. Luque-Centeno, M.V. Martínez-Huerta, D. Sebastián, G. Lemes, E. Pastor, M. J. Lázaro, Bifunctional N-doped graphene Ti and Co nanocomposites for the oxygen reduction and evolution reactions, Renew. Energy. 125 (2018) 182–192, https://doi.org/10.1016/J.RENENE.2018.02.073.
[28] V.C.A. Ficca, C. Santoro, A. D'Epifanio, S. Licoccia, A. Serov, P. Atanassov, B. Mecheri, Effect of active site poisoning on iron−nitrogen−carbon platinum-group-metal-free oxygen reduction reaction catalysts operating in neutral media: a rotating disk electrode study, ChemElectroChem. 7 (2020) 3044–3055, https://doi.org/10.1002/celc.202000754.
[29] B. Mecheri, R. Gokhale, C. Santoro, M.A. Costa De Oliveira, A. D'Epifanio, S. Licoccia, A. Serov, K. Artyushkova, P. Atanassov, Oxygen reduction reaction electrocatalysts derived from iron salt and benzimidazole and aminobenzimidazole precursors and their application in microbial fuel cell cathodes, ACS Appl. Energy Mater. 1 (2018) 5755–5765, https://doi.org/10.1021/acsaem.8b01360.

[30] W. da Silva Freitas, P.P. Machado Pico, A. D'Epifanio, B. Mecheri, Nanostructured Fe-N-C as bifunctional catalysts for oxygen reduction and hydrogen evolution, Catalysts. 11 (2021) 1525, https://doi.org/10.3390/catal11121525.

[31] L. Osmieri, Transition metal–nitrogen–carbon (M–N–C) catalysts for oxygen reduction reaction. Insights on synthesis and performance in polymer electrolyte fuel cells, ChemEngineering. 3 (2019) 1–32, https://doi.org/10.3390/chemengineering3010016.

[32] L. Osmieri, R. Escudero-Cid, M. Armandi, P. Ocón, A.H.A. Monteverde Videla, S. Specchia, Effects of using two transition metals in the synthesis of non-noble electrocatalysts for oxygen reduction reaction in direct methanol fuel cell, Electrochim. Acta. 266 (2018) 220–232, https://doi.org/10.1016/J.ELECTACTA.2018.02.036.

[33] P. Rao, D. Wu, T.-J. Wang, J. Li, P. Deng, Q. Chen, Y. Shen, Y. Chen, X. Tian, Single atomic cobalt electrocatalyst for efficient oxygen reduction reaction, EScience. 2 (2022) 399–404, https://doi.org/10.1016/j.esci.2022.05.004.

[34] P. Rao, Y. Deng, W. Fan, J. Luo, P. Deng, J. Li, Y. Shen, X. Tian, Movable type printing method to synthesize high-entropy single-atom catalysts, Nat. Commun. 13 (2022) 5071, https://doi.org/10.1038/s41467-022-32850-8.

[35] P. Rao, D. Wu, J. Luo, J. Li, P. Deng, Y. Shen, X. Tian, A plasma bombing strategy to synthesize high-loading single-atom catalysts for oxygen reduction reaction, Cell Reports Phys. Sci. 3 (5) (2022) 100880.

[36] R. Gokhale, Y. Chen, A. Serov, K. Artyushkova, P. Atanassov, Direct synthesis of platinum group metal-free Fe-N-C catalyst for oxygen reduction reaction in alkaline media, Electrochem. Commun. 72 (2016) 140–143, https://doi.org/10.1016/j.elecom.2016.09.013.

[37] M.M. Hossen, K. Artyushkova, P. Atanassov, A. Serov, Synthesis and characterization of high performing Fe-N-C catalyst for oxygen reduction reaction (ORR) in Alkaline Exchange Membrane Fuel Cells, J. Power Sources. 375 (2018) 214–221, https://doi.org/10.1016/j.jpowsour.2017.08.036.

[38] R. Gokhale, Y. Chen, A. Serov, K. Artyushkova, P. Atanassov, Novel dual templating approach for preparation of highly active Fe-N-C electrocatalyst for oxygen reduction, Electrochim. Acta. 224 (2017) 49–55, https://doi.org/10.1016/j.electacta.2016.12.052.

[39] Y. Zheng, F. He, J. Wu, D. Ma, H. Fan, S. Zhu, X. Li, Y. Lu, Q. Liu, X. Hu, Nitrogen-doped carbon nanotube-graphene frameworks with encapsulated fe/fe3n nanoparticles as catalysts for oxygen reduction, ACS Appl. Nano Mater. 2 (2019) 3538–3547, https://doi.org/10.1021/acsanm.9b00506.

[40] I. Martinaiou, A.H.A. Monteverde Videla, N. Weidler, M. Kübler, W.D.Z. Wallace, S. Paul, S. Wagner, A. Shahraei, R.W. Stark, S. Specchia, U.I. Kramm, Activity and degradation study of an Fe-N-C catalyst for ORR in Direct Methanol Fuel Cell (DMFC), Appl. Catal. B Environ. 262 (2020), 118217, https://doi.org/10.1016/J.APCATB.2019.118217.

[41] L. Osmieri, R. Escudero-Cid, A.H.A. Monteverde Videla, P. Ocón, S. Specchia, Application of a non-noble Fe-N-C catalyst for oxygen reduction reaction in an alkaline direct ethanol fuel cell, Renew Energy. 115 (2018) 226–237, https://doi.org/10.1016/J.RENENE.2017.08.062.

[42] A.H.A. Monteverde Videla, L. Osmieri, M. Armandi, S. Specchia, Varying the morphology of Fe-N-C electrocatalysts by templating Iron phthalocyanine precursor with different porous SiO2 to promote the oxygen reduction reaction, Electrochim. Acta. 177 (2015) 43–50, https://doi.org/10.1016/j.electacta.2015.01.165.

[43] L. Osmieri, R. Escudero-Cid, A.H.A. Monteverde Videla, P. Ocón, S. Specchia, Performance of a Fe-N-C catalyst for the oxygen reduction reaction in direct methanol fuel cell: cathode formulation optimization and short-term durability, Appl. Catal. B Environ. 201 (2017) 253–265, https://doi.org/10.1016/j.apcatb.2016.08.043.

[44] L. Osmieri, R. Escudero-cid, M. Armandi, A.H.A. Monteverde, J. Luís, G. Fierro, P. Ocón, S. Specchia, Applied catalysis B: environmental Fe-N / C catalysts for oxygen reduction reaction supported on different carbonaceous materials. performance in acidic and alkaline direct alcohol fuel cells, Appl. Catal. B, Environ. 205 (2017) 637–653, https://doi.org/10.1016/j.apcatb.2017.01.003.

[45] W. Yang, X. Wang, R. Rossi, B.E. Logan, Low-cost Fe–N–C catalyst derived from Fe (III)-chitosan hydrogel to enhance power production in microbial fuel cells, Chem. Eng. J. 380 (2020), 122522, https://doi.org/10.1016/j.cej.2019.122522.

[46] S. Rojas-Carbonell, K. Artyushkova, A. Serov, C. Santoro, I. Matanovic, P. Atanassov, Effect of pH on the activity of platinum group metal-free catalysts in oxygen reduction reaction, ACS Catal. 8 (2018) 3041–3053, https://doi.org/10.1021/acscatal.7b03991.

[47] T. Asset, P. Atanassov, Iron-nitrogen-carbon catalysts for proton exchange membrane fuel cells, Joule. 4 (2020) 33–44, https://doi.org/10.1016/j.joule.2019.12.002.

[48] S.S.A. Shah, T. Najam, C. Molochas, M.A. Nazir, A. Brouzgou, M.S. Javed, A. Ur Rehman, P. Tsiakaras, Nanostructure engineering of metal–organic derived frameworks: cobalt phosphide embedded in carbon nanotubes as an efficient orr catalyst, Molecules. 26 (2021) 1–11, https://doi.org/10.3390/molecules26216672.

[49] S.S.A. Shah, T. Najam, M.K. Aslam, M. Ashfaq, M.M. Rahman, K. Wang, P. Tsiakaras, S. Song, Y. Wang, Recent advances on oxygen reduction electrocatalysis: correlating the characteristic properties of metal organic frameworks and the derived nanomaterials, Appl. Catal. B Environ. 268 (2020), 118570, https://doi.org/10.1016/J.APCATB.2019.118570.

[50] F. Lu, K. Fan, L. Cui, Y. Yang, W. Wang, G. Zhang, C. Wang, Q. Zhang, B. Li, L. Zong, L. Wang, Cu-N4 single atoms derived from metal-organic frameworks with trapped nitrogen-rich molecules and their use as efficient electrocatalysts for oxygen reduction reaction, Chem. Eng. J. 431 (2022), 133242, https://doi.org/10.1016/J.CEJ.2021.133242.

[51] D.L. Zhao, F. Feng, L. Shen, Z. Huang, Q. Zhao, H. Lin, T.S. Chung, Engineering metal–organic frameworks (MOFs) based thin-film nanocomposite (TFN) membranes for molecular separation, Chem. Eng. J. 454 (2023), 140447, https://doi.org/10.1016/J.CEJ.2022.140447.

[52] L. Yan, A. Gopal, S. Kashif, P. Hazelton, M. Lan, W. Zhang, X. Chen, Metal organic frameworks for antibacterial applications, Chem. Eng. J. 435 (2022), 134975, https://doi.org/10.1016/J.CEJ.2022.134975.

[53] Y. Zhang, B. Wang, R. Wang, Functionally decorated metal–organic frameworks in environmental remediation, Chem. Eng. J. 455 (2023), 140741, https://doi.org/10.1016/J.CEJ.2022.140741.

[54] H.M. Barkholtz, D.J. Liu, Advancements in rationally designed PGM-free fuel cell catalysts derived from metal-organic frameworks, Mater. Horizons. 4 (2017) 20–37, https://doi.org/10.1039/c6mh00344c.

[55] W. da Silva Freitas, B. Mecheri, C. Lo Vecchio, I. Gatto, V. Baglio, V.C.A. Ficca, A. Patra, E. Placidi, A. D'Epifanio, Metal-organic-framework-derived electrocatalysts for alkaline polymer electrolyte fuel cells, J. Power Sources. 550 (2022), 232135, https://doi.org/10.1016/J.JPOWSOUR.2022.232135.

[56] B. Liu, H. Shioyama, T. Akita, Q. Xu, Metal-organic framework as a template for porous carbon synthesis, J. Am. Chem. Soc. 130 (2008) 5390–5391, https://doi.org/10.1021/ja7106146.

[57] F. Jaouen, S. Marcotte, J.P. Dodelet, G. Lindbergh, Oxygen reduction catalysts for polymer electrolyte fuel cells from the pyrolysis of iron acetate adsorbed on various carbon supports, J. Phys. Chem. B. 107 (2003) 1376–1386, https://doi.org/10.1021/jp021634q.

[58] B. Ricciardi, B. Mecheri, W. da Silva Freitas, V.C.A. Ficca, E. Placidi, I. Gatto, A. Carbone, A. Capasso, A. D'Epifanio, Porous Iron-Nitrogen-Carbon Electrocatalysts for Anion Exchange Membrane Fuel Cells (AEMFC), Porous Iron-Nitrogen-Carbon Electrocatalysts for Anion Exchange Membrane Fuel Cells (AEMFC) 10 (7) (2023), https://doi.org/10.1002/celc.202201115.

[59] W.d.S. Freitas, A. D'Epifanio, V.C.A. Ficca, E. Placidi, F. Arciprete, B. Mecheri, Tailoring active sites of iron-nitrogen-carbon catalysts for oxygen reduction in alkaline environment: effect of nitrogen-based organic precursor and pyrolysis atmosphere, Electrochim. Acta. 391 (2021) 138899.

[60] A. Iannaci, B. Mecheri, A. D'Epifanio, M.J. Lázaro Elorri, S. Licoccia, Iron–nitrogen-functionalized carbon as efficient oxygen reduction reaction electrocatalyst in microbial fuel cells, Int. J. Hydrogen Energy. 41 (2016) 19637–19644, https://doi.org/10.1016/j.ijhydene.2016.04.154.

[61] S. Rojas-Carbonell, C. Santoro, A. Serov, P. Atanassov, Transition metal-nitrogen-carbon catalysts for oxygen reduction reaction in neutral electrolyte, Electrochem. Commun. 75 (2017) 38–42, https://doi.org/10.1016/j.elecom.2016.12.011.

[62] C.A. Campos-Roldán, R.G. González-Huerta, N. Alonso-Vante, Experimental protocol for hor and orr in alkaline electrochemical measurements, J. Electrochem. Soc. 165 (2018) J3001–J3007, https://doi.org/10.1149/2.0011815jes.

[63] C. Lafforgue, F. Maillard, V. Martin, L. Dubau, M. Chatenet, Degradation of carbon-supported platinum-group-metal electrocatalysts in alkaline media studied by in situ fourier transform infrared spectroscopy and identical-location transmission electron microscopy, ACS Catal. 9 (6) (2019) 5613–5622.

[64] A. Ohma, K. Shinohara, A. Iiyama, T. Yoshida, A. Daimaru, Membrane and catalyst performance targets for automotive fuel cells by fccj membrane, Catalyst, MEA WG ECS Trans. 41 (2019) 775–784, https://doi.org/10.1149/1.3635611.

[65] C. Lo Vecchio, D. Sebastián, M.J. Lázaro, A.S. Aricò, V. Baglio, Methanol-tolerant m–n–c catalysts for oxygen reduction reactions in acidic media and their application in direct methanol fuel cells, Catalysts. 8 (2018) 1–14, https://doi.org/10.3390/catal8120650.

[66] I. Gatto, A. Caprì, C. Lo Vecchio, S. Zignani, A. Patti, V. Baglio, Optimal operating conditions evaluation of an anion-exchange-membrane electrolyzer based on FUMASEP® FAA3-50 membrane, Int. J. Hydrogen Energy. 48 (32) (2023) 11914–11921.

[67] I. Gatto, A. Patti, A. Carbone, Assessment of the FAA3-50 polymer electrolyte for anion exchange membrane fuel cells, ChemElectroChem. 202201052 (2022) 1–7, https://doi.org/10.1002/celc.202201052.

[68] P. Arabkhani, H. Javadian, A. Asfaram, M. Ateia, Decorating graphene oxide with zeolitic imidazolate framework (ZIF-8) and pseudo-boehmite offers ultra-high adsorption capacity of diclofenac in hospital effluents, Chemosphere. 271 (2021), 129610, https://doi.org/10.1016/j.chemosphere.2021.129610.

[69] Y. Hu, Z. Liu, J. Xu, Y. Huang, Y. Song, Evidence of pressure enhanced CO2 storage in ZIF-8 probed by FTIR spectroscopy, J. Am. Chem. Soc. 135 (2013) 9287–9290, https://doi.org/10.1021/ja403635b.

[70] Y. Ye, Y.A. Elabd, Relative chemical stability of imidazolium-based alkaline anion exchange polymerized ionic liquids, Macromolecules. 44 (2011) 8494–8503, https://doi.org/10.1021/ma201864u.

[71] K.S. Park, Z. Ni, A.P. Côté, J.Y. Choi, R. Huang, F.J. Uribe-Romo, H.K. Chae, M. O'Keeffe, O.M. Yaghi, Exceptional chemical and thermal stability of zeolitic imidazolate frameworks, Proc. Natl. Acad. Sci. U. S. A. 103 (2006) 10186–10191, https://doi.org/10.1073/pnas.0602439103.

[72] J.B. James, Y.S. Lin, Kinetics of ZIF-8 thermal decomposition in inert, oxidizing, and reducing environments, J. Phys. Chem. C. 120 (2016) 14015–14026, https://doi.org/10.1021/acs.jpcc.6b01208.

[73] Z. Abbasi, E. Shamsaei, S.K. Leong, B. Ladewig, X. Zhang, H. Wang, Effect of carbonization temperature on adsorption property of ZIF-8 derived nanoporous carbon for water treatment, Microporous Mesoporous Mater. 236 (2016) 28–37, https://doi.org/10.1016/j.micromeso.2016.08.022.

[74] E.A. Fletcher, Solarthermal and solar quasi-electrolytic processing and separations: Zinc from zinc oxide as an example, Ind. Eng. Chem. Res. 38 (1999) 2275–2282, https://doi.org/10.1021/ie990053t.
[75] D. Angin, Effect of pyrolysis temperature and heating rate on biochar obtained from pyrolysis of safflower seed press cake, Bioresour. Technol. 128 (2013) 593–597, https://doi.org/10.1016/j.biortech.2012.10.150.
[76] H. Ling Poh, P. Šimek, Z. Sofer, M. Pumera, Sulfur-doped graphene via thermal exfoliation of graphite oxide in H2S, SO2, or CS2 Gas, ACS Nano. 7 (2013) 5262–5272, https://doi.org/10.1021/nn401296b.
[77] A. Fujimoto, Y. Yamada, M. Koinuma, S. Sato, Origins of sp3C peaks in C1s X-ray photoelectron spectra of carbon materials, Anal. Chem. 88 (2016) 6110–6114, https://doi.org/10.1021/acs.analchem.6b01327.
[78] B. Mecheri, V.C.A. Ficca, M.A. Costa de Oliveira, A. D'Epifanio, E. Placidi, F. Arciprete, S. Licoccia, Facile synthesis of graphene-phthalocyanine composites as oxygen reduction electrocatalysts in microbial fuel cells, Appl. Catal. B Environ. 237 (2018) 699–707, https://doi.org/10.1016/j.apcatb.2018.06.031.
[79] K. Artyushkova, S. Rojas-Carbonell, C. Santoro, E. Weiler, A. Serov, R. Awais, R. Rajeev Gokhale, P. Atanassov, Correlations between synthesis and performance of fe-based pgm-free catalysts in acidic and alkaline media: evolution of surface chemistry and morphology, ACS Appl. Energy Mater. 2 (2019) 5406–5418, https://doi.org/10.1021/acsaem.9b00331.
[80] M. Smith, L. Scudiero, J. Espinal, J.S. McEwen, M. Garcia-Perez, Improving the deconvolution and interpretation of XPS spectra from chars by ab initio calculations, Carbon N. Y. 110 (2016) 155–171, https://doi.org/10.1016/J.CARBON.2016.09.012.
[81] M. Guzzo, J.J. Kas, L. Sponza, C. Giorgetti, F. Sottile, D. Pierucci, M.G. Silly, F. Sirotti, J.J. Rehr, L. Reining, Multiple satellites in materials with complex plasmon spectra: From graphite to graphene, Phys. Rev. B. 89 (2014), 085425, https://doi.org/10.1103/PhysRevB.89.085425.
[82] I. Matanovic, K. Artyushkova, P. Atanassov, Understanding PGM-free catalysts by linking density functional theory calculations and structural analysis: Perspectives and challenges, Curr. Opin. Electrochem. 9 (2018) 137–144, https://doi.org/10.1016/j.coelec.2018.03.009.
[83] I. Matanovic, K. Artyushkova, M.B. Strand, M.J. Dzara, S. Pylypenko, P. Atanassov, Core level shifts of hydrogenated pyridinic and pyrrolic nitrogen in the nitrogen-containing graphene-based electrocatalysts: in-plane vs edge defects, J. Phys. Chem. C. 120 (2016) 29225–29232, https://doi.org/10.1021/acs.jpcc.6b09778.
[84] K. Artyushkova, A. Serov, S. Rojas-Carbonell, P. Atanassov, Chemistry of multitudinous active sites for oxygen reduction reaction in transition metal-nitrogen-carbon electrocatalysts, J. Phys. Chem. C. 119 (2015) 25917–25928, https://doi.org/10.1021/acs.jpcc.5b07653.
[85] V.C.A. Ficca, C. Santoro, E. Placidi, F. Arciprete, A. Serov, P. Atanassov, B. Mecheri, Exchange current density as an effective descriptor of poisoning of active sites in platinum group metal-free electrocatalysts for oxygen reduction reaction, ACS Catal. 13 (4) (2023) 2162–2175.
[86] K. Artyushkova, C. Walker, W. Patterson, P. Atanassov, Hierarchically structured non-pgm oxygen reduction electrocatalyst based on microemulsion-templated silica and pyrolyzed iron and cyanamide precursors, Electrocatalysis. 5 (2014) 241–247, https://doi.org/10.1007/s12678-014-0185-2.
[87] Y. He, H. Guo, S. Hwang, X. Yang, Z. He, J. Braaten, S. Karakalos, W. Shan, M. Wang, H. Zhou, Z. Feng, K.L. More, G. Wang, D. Su, D.A. Cullen, L. Fei, S. Litster, G. Wu, Single cobalt sites dispersed in hierarchically porous nanofiber networks for durable and high-power pgm-free cathodes in fuel cellstitle, Adv. Mater. 32 (2020) 2003577, https://doi.org/10.1002/adma.202003577.
[88] K. Artyushkova, S. Rojas-Carbonell, C. Santoro, E. Weiler, A. Serov, R. Awais, R. R. Gokhale, P. Atanassov, Correlations between synthesis and performance of fe-based pgm-free catalysts in acidic and alkaline media: evolution of surface chemistry and morphology, ACS Appl. Energy Mater. 2 (2019) 5406–5418, https://doi.org/10.1021/acsaem.9b00331.
[89] K. Artyushkova, I. Matanovic, B. Halevi, P. Atanassov, Oxygen binding to active sites of fe–n–c orr electrocatalysts observed by ambient-pressure xpS, J. Phys. Chem. C. 121 (2017) 2836–2843, https://doi.org/10.1021/acs.jpcc.6b11721.
[90] X. Yin, H.T. Chung, U. Martinez, L. Lin, K. Artyushkova, P. Zelenay, PGM-Free ORR catalysts designed by templating pani-type polymers containing functional groups with high affinity to iron, J. Electrochem. Soc. 166 (2019) F3240–F3245, https://doi.org/10.1149/2.0301907jes.
[91] M. Kodali, C. Santoro, A. Serov, S. Kabir, K. Artyushkova, I. Matanovic, P. Atanassov, Air breathing cathodes for microbial fuel cell using mn-, fe-, co- and ni-containing platinum group metal-free catalysts, Electrochim. Acta. 231 (2017) 115–124, https://doi.org/10.1016/j.electacta.2017.02.033.
[92] L. Lin, Z. Kun Yang, Y.-F. Jiang, A.-W. Xu, Nonprecious bimetallic (fe, mo)–n/c catalyst for efficient oxygen reduction reaction, ACS Catal. 6 (2016) 4449–4454, https://doi.org/10.1021/acscatal.6b00535.
[93] A. Serov, K. Artyushkova, P. Atanassov, Fe-N-C oxygen reduction fuel cell catalyst derived from carbendazim: synthesis, structure, and reactivity, Adv. Energy Mater. 4 (2014) 1–7, https://doi.org/10.1002/aenm.201301735.
[94] E.R. Edwards, E.F. Antunes, E.C. Botelho, M.R. Baldan, E.J. Corat, Evaluation of residual iron in carbon nanotubes purified by acid treatments, Appl. Surf. Sci. 258 (2011) 641–648, https://doi.org/10.1016/J.APSUSC.2011.07.032.
[95] L. Niu, X. Liu, X. Zhou, C. Huo, J. Xu, X. Wen, J.W. Niemantsverdriet, Y. Yang, Y. Li, Genesis of an Fe5C2@Fe3O4 core/shell structure during CO carburization of metallic iron nanoparticles, J. Catal. 407 (2022) 97–103, https://doi.org/10.1016/J.JCAT.2022.01.029.
[96] R. Ahmad, U.A. Khan, N. Iqbal, T. Noor, Zeolitic imidazolate framework (ZIF)-derived porous carbon materials for supercapacitors: an overview, RSC Adv. 10 (2020) 43733–43750, https://doi.org/10.1039/d0ra08560j.
[97] P. Chandran, A. Ghosh, S. Ramaprabhu, High-performance Platinum-free oxygen reduction reaction and hydrogen oxidation reaction catalyst in polymer electrolyte membrane fuel cell, Sci. Rep. 8 (2018) 1–11, https://doi.org/10.1038/s41598-018-22001-9.
[98] U. Martinez, E.F. Holby, S.K. Babu, K. Artyushkova, L. Lin, S. Choudhury, G. M. Purdy, P. Zelenay, Experimental and theoretical trends of pgm-free electrocatalysts for the oxygen reduction reaction with different transition metals, J. Electrochem. Soc. 166 (2019) F3136–F3142, https://doi.org/10.1149/2.0201907jes.
[99] N. Ramaswamy, U. Tylus, Q. Jia, S. Mukerjee, Activity descriptor identification for oxygen reduction on nonprecious electrocatalysts: Linking surface science to coordination chemistry, J. Am. Chem. Soc. 135 (2013) 15443–15449, https://doi.org/10.1021/ja405149m.
[100] E. Yeager, Electrocatalysts for O2 reduction, Electrochim. Acta. 29 (1984) 1527–1537, https://doi.org/10.1016/0013-4686(84)85006-9.
[101] M.V. Castegnaro, W.J. Paschoalino, M.R. Fernandes, B. Balke, M.C.M. Alves, E. A. Ticianelli, J. Morais, Pd-M/C (M = Pd, Cu, Pt) electrocatalysts for oxygen reduction reaction in alkaline medium: correlating the electronic structure with activity, Langmuir. 33 (2017) 2734–2743, https://doi.org/10.1021/acs.langmuir.7b00098.
[102] R. Guidelli, R.G. Compton, J.M. Feliu, E. Gileadi, J. Lipkowski, W. Schmickler, S. Trasatti, Definition of the transfer coefficient in electrochemistry (IUPAC recommendations 2014), Pure Appl. Chem. 86 (2) (2014) 259–262.
[103] L. Osmieri, A.H.A. Monteverde Videla, S. Specchia, The use of different types of reduced graphene oxide in the preparation of Fe-N-C electrocatalysts: capacitive behavior and oxygen reduction reaction activity in alkaline medium, J. Solid State Electrochem. 20 (2016) 3507–3523, https://doi.org/10.1007/s10008-016-3332-2.
[104] A. Holewinski, S. Linic, Elementary mechanisms in electrocatalysis: revisiting the orr tafel slope, J. Electrochem. Soc. 159 (2012) H864–H870, https://doi.org/10.1149/2.022211jes.
[105] J. Perez, E.R. Gonzalez, E.A. Ticianelli, Oxygen electrocatalysis on thin porous coating rotating platinum electrodes, Electrochim. Acta. 44 (1998) 1329–1339, https://doi.org/10.1016/S0013-4686(98)00255-2.
[106] T. Shinagawa, A.T. Garcia-Esparza, K. Takanabe, Insight on tafel slopes from a microkinetic analysis of aqueous electrocatalysis for energy conversion, Sci. Rep. 5 (2015) 1–21, https://doi.org/10.1038/srep13801.
[107] F. Jaouen, O2 reduction mechanism on non-noble metal catalysts for PEM fuel cells. Part II: a porous-electrode model to predict the quantity of H 2O2 detected by rotating ring-diskelectrode, J. Phys. Chem. C. 113 (2009) 15433–15443, https://doi.org/10.1021/jp900838x.
[108] F. Jaouen, J.P. Dodelet, O2 reduction mechanism on non-noble metal catalysts for PEM fuel cells. part I: experimental rates of O2 electroreduction, H 2O2 electroreduction, and H2O2 disproportionation, J. Phys. Chem. C. 113 (2009) 15422–15432, https://doi.org/10.1021/jp900837e.
[109] W.E. Mustain, M. Chatenet, M. Page, Y.S. Kim, Durability challenges of anion exchange membrane fuel cells, Energy Environ. Sci. 13 (2020) 2805–2838, https://doi.org/10.1039/d0ee01133a.
[110] I. Martinaiou, T. Wolker, A. Shahraei, G.R. Zhang, A. Janßen, S. Wagner, N. Weidler, R.W. Stark, B.J.M. Etzold, U.I. Kramm, Improved electrochemical performance of Fe-N-C catalysts through ionic liquid modification in alkaline media, J. Power Sources. 375 (2018) 222–232, https://doi.org/10.1016/j.jpowsour.2017.07.028.
[111] F. Jaouen, J. Herranz, M. Lefévre, J.P. Dodelet, U.I. Kramm, I. Herrmann, P. Bogdanoff, J. Maruyama, T. Nagaoka, A. Garsuch, J.R. Dahn, T. Olson, S. Pylypenko, P. Atanassov, E.A. Ustinov, Cross-laboratory experimental study of non-noble-metal electrocatalysts for the oxygen reduction reaction, ACS Appl. Mater. Interfaces. 1 (2009) 1623–1639, https://doi.org/10.1021/am900219g.
[112] R.K. Singh, R. Devivaraprasad, T. Kar, A. Chakraborty, M. Neergat, Electrochemical impedance spectroscopy of oxygen reduction reaction (orr) in a rotating disk electrode configuration: effect of ionomer content and carbon-support, J. Electrochem. Soc. 162 (2015) F489–F498, https://doi.org/10.1149/2.0141506jes.
[113] D. Sebastián, A. Serov, K. Artyushkova, P. Atanassov, A.S. Aricò, V. Baglio, Performance, methanol tolerance and stability of Fe-aminobenzimidazole derived catalyst for direct methanol fuel cells, J. Power Sources. 319 (2016) 235–246, https://doi.org/10.1016/j.jpowsour.2016.04.067.
[114] S. Ratso, I. Kruusenberg, M. Käärik, M. Kook, R. Saar, P. Kanninen, T. Kallio, J. Leis, K. Tammeveski, Transition metal-nitrogen co-doped carbide-derived carbon catalysts for oxygen reduction reaction in alkaline direct methanol fuel cell, Appl. Catal. B Environ. 219 (2017) 276–286, https://doi.org/10.1016/J.APCATB.2017.07.036.
[115] S. Ratso, I. Kruusenberg, A. Sarapuu, P. Rauwel, R. Saar, U. Joost, J. Aruväli, P. Kanninen, T. Kallio, K. Tammeveski, Enhanced oxygen reduction reaction activity of iron-containing nitrogen-doped carbon nanotubes for alkaline direct methanol fuel cell application, J. Power Sources. 332 (2016) 129–138, https://doi.org/10.1016/j.jpowsour.2016.09.069.
[116] X. Li, B.N. Popov, T. Kawahara, H. Yanagi, Non-precious metal catalysts synthesized from precursors of carbon, nitrogen, and transition metal for oxygen reduction in alkaline fuel cells, J. Power Sources. 196 (2011) 1717–1722, https://doi.org/10.1016/j.jpowsour.2010.10.018.
[117] C. Chen, X.D. Yang, Z.Y. Zhou, Y.J. Lai, M. Rauf, Y. Wang, J. Pan, L. Zhuang, Q. Wang, Y.C. Wang, N. Tian, X.S. Zhang, S.G. Sun, Aminothiazole-derived N, S,

Fe-doped graphene nanosheets as high performance electrocatalysts for oxygen reduction, Chem. Commun. 51 (2015) 17092–17095, https://doi.org/10.1039/c5cc06562c.
[118] S. Hanif, N. Iqbal, X. Shi, T. Noor, G. Ali, A.M. Kannan, NiCo–N-doped carbon nanotubes based cathode catalyst for alkaline membrane fuel cell, Renew. Energy. 154 (2020) 508–516, https://doi.org/10.1016/j.renene.2020.03.060.
[119] V.M. Dhavale, S.K. Singh, A. Nadeema, S.S. Gaikwad, A.S. Kurungot, Nanocrystalline Fe-Fe2O3 particle-deposited n-doped graphene as an activity modulated pt-free electrocatalyst for oxygen reduction reaction, Nanoscale. 7 (2015) 20117–20125, https://doi.org/10.1039/C5NR04929F.
[120] P. Teppor, R. Jäger, M. Paalo, A. Adamson, M. Härmas, O. Volobujeva, J. Aruväli, R. Palm, E. Lust, Peat as a carbon source for non-platinum group metal oxygen electrocatalysts and AEMFC cathodes, Int. J. Hydrogen Energy. 47 (2022) 16908–16920, https://doi.org/10.1016/j.ijhydene.2022.03.199.
[121] H.S. Kim, C.H. Lee, J.H. Jang, M.S. Kang, H. Jin, K.S. Lee, S.U. Lee, S.J. Yoo, W. C. Yoo, Single-atom oxygen reduction reaction electrocatalysts of Fe, Si, and N co-doped carbon with 3D interconnected mesoporosity, J. Mater. Chem. A. 9 (2021) 4297–4309, https://doi.org/10.1039/d0ta11208a.
[122] C.L. Vecchio, X. Lyu, I. Gatto, B. Zulevi, A. Serov, V. Baglio, C.L. Vecchio, I. Gatto, V. Baglio, Performance investigation of alkaline direct methanol fuel cell with commercial PGM-free cathodic materials, J. Power Sources. 561 (2023) 232732.
[123] G.K.S. Prakash, F.C. Krause, F.A. Viva, S.R. Narayanan, G.A. Olah, Study of operating conditions and cell design on the performance of alkaline anion exchange membrane based direct methanol fuel cells, J. Power Sources. 196 (2011) 7967–7972, https://doi.org/10.1016/j.jpowsour.2011.05.056.
[124] P.F. Msomi, P.T. Nonjola, P.G. Ndungu, J. Ramontja, Poly (2, 6-dimethyl-1, 4-phenylene)/polysulfone anion exchange membrane blended with TiO2 with improved water uptake for alkaline fuel cell application, Int. J. Hydrogen Energy. 45 (2020) 29465–29476, https://doi.org/10.1016/j.ijhydene.2020.08.012.
[125] K. Ai, Z. Li, X. Cui, Scalable preparation of sized-controlled Co-N-C electrocatalyst for efficient oxygen reduction reaction, J. Power Sources. 368 (2017) 46–56, https://doi.org/10.1016/J.JPOWSOUR.2017.09.067.
[126] S. Ratso, I. Kruusenberg, M. Käärik, M. Kook, L. Puust, R. Saar, J. Leis, K. Tammeveski, Highly efficient transition metal and nitrogen co-doped carbide-derived carbon electrocatalysts for anion exchange membrane fuel cells, J. Power Sources. 375 (2018) 233–243, https://doi.org/10.1016/J.JPOWSOUR.2017.08.046.
[127] R. Praats, M. Käärik, A. Kikas, V. Kisand, J. Aruväli, P. Paiste, M. Merisalu, J. Leis, V. Sammelselg, J.H. Zagal, S. Holdcroft, N. Nakashima, K. Tammeveski, Electrocatalytic oxygen reduction reaction on iron phthalocyanine-modified carbide-derived carbon/carbon nanotube composite electrocatalysts, Electrochim. Acta. 334 (2020) 135575.
[128] J. Lilloja, M. Mooste, E. Kibena-Põldsepp, A. Sarapuu, B. Zulevi, A. Kikas, H.-M. Piirsoo, A. Tamm, V. Kisand, S. Holdcroft, A. Serov, K. Tammeveski, Mesoporous iron-nitrogen co-doped carbon material as cathode catalyst for the anion exchange membrane fuel cell, J. Power Sources Adv. 8 (2021) 100052.
[129] R. Sibul, E. Kibena-Põldsepp, S. Ratso, M. Kook, M.T. Sougrati, M. Käärik, M. Merisalu, J. Aruväli, P. Paiste, A. Treshchalov, J. Leis, V. Kisand, V. Sammelselg, S. Holdcroft, F. Jaouen, K. Tammeveski, Iron- and nitrogen-doped graphene-based catalysts for fuel cell applications, ChemElectroChem. 7 (2020) 1739–1747, https://doi.org/10.1002/celc.202000011.
[130] S. Ratso, A. Zitolo, M. Käärik, M. Merisalu, A. Kikas, V. Kisand, M. Rähn, P. Paiste, J. Leis, V. Sammelselg, S. Holdcroft, F. Jaouen, K. Tammeveski, Non-precious metal cathodes for anion exchange membrane fuel cells from ball-milled iron and nitrogen doped carbide-derived carbons, Renew. Energy. 167 (2021) 800–810, https://doi.org/10.1016/j.renene.2020.11.154.